Cerebral Cortex, March 2020;30: 969–988

doi: 10.1093/cercor/bhz141
Advance Access Publication Date: 29 July 2019
Original Article

ORIGINAL ARTICLE

Deletion of *Fmr1* from Forebrain Excitatory Neurons Triggers Abnormal Cellular, EEG, and Behavioral Phenotypes in the Auditory Cortex of a Mouse Model of Fragile X Syndrome

Jonathan W. Lovelace[1,†], Maham Rais[2,†], Arnold R. Palacios[2], Xinghao S. Shuai[2], Steven Bishay[2], Otilia Popa[2], Patricia S. Pirbhoy[2], Devin K. Binder[2,3], David L. Nelson[4], Iryna M. Ethell[2,3,*] and Khaleel A. Razak[1,3,*]

[1]Department of Psychology, [2]Division of Biomedical Sciences, School of Medicine, [3]Graduate Neuroscience Program, University of California Riverside, Riverside, CA 92521,USA and [4]Molecular and Human Genetics, Baylor College of Medicine , Houston, TX 77030, USA

Address correspondence to Khaleel A. Razak, Department of Psychology, University of California Riverside, Riverside, CA 92521, USA. Email: Khaleel@ucr.edu; Iryna M. Ethell, Division of Biomedical Sciences, School of Medicine, University of California Riverside, Riverside, CA 92521, USA. Email: iryna.ethell@medsch.ucr.edu.

[†]Jonathan W. Lovelace and Maham Rais authors have contributed equally to this work

Abstract

Fragile X syndrome (FXS) is a leading genetic cause of autism with symptoms that include sensory processing deficits. In both humans with FXS and a mouse model [*Fmr1* knockout (KO) mouse], electroencephalographic (EEG) recordings show enhanced resting state gamma power and reduced sound-evoked gamma synchrony. We previously showed that elevated levels of matrix metalloproteinase-9 (MMP-9) may contribute to these phenotypes by affecting perineuronal nets (PNNs) around parvalbumin (PV) interneurons in the auditory cortex of *Fmr1* KO mice. However, how different cell types within local cortical circuits contribute to these deficits is not known. Here, we examined whether *Fmr1* deletion in forebrain excitatory neurons affects neural oscillations, MMP-9 activity, and PV/PNN expression in the auditory cortex. We found that cortical MMP-9 gelatinase activity, mTOR/Akt phosphorylation, and resting EEG gamma power were enhanced in $Cre^{Nex1}/Fmr1^{Flox/y}$ conditional KO (cKO) mice, whereas the density of PV/PNN cells was reduced. The $Cre^{Nex1}/Fmr1^{Flox/y}$ cKO mice also show increased locomotor activity, but not the anxiety-like behaviors. These results indicate that fragile X mental retardation protein changes in excitatory neurons in the cortex are sufficient to elicit cellular, electrophysiological, and behavioral phenotypes in *Fmr1* KO mice. More broadly, these results indicate that local cortical circuit abnormalities contribute to sensory processing deficits in autism spectrum disorders.

Key words: autism, cortical deficits, fragile X syndrome, perineuronal nets, sensory processing disorders

Introduction

Fragile X syndrome (FXS) is a common monogenic form of autism spectrum disorders (ASD) (Crawford et al. 2001). FXS is usually caused by a CGG repeat expansion in 5′-untranslated region of the *Fragile X mental retardation 1* (*Fmr1*) *gene* with consequent gene methylation, downregulation of fragile X mental retardation protein (FMRP), translational dysregulation, and abnormal protein synthesis (Verkerk et al. 1991; Sutcliffe et al. 1992). Symptoms of FXS include anxiety, intellectual disability, repetitive behaviors, social communication deficits, and abnormal sensory processing (Penagarikano et al. 2007; Braat and Kooy 2015). Abnormal sensory processing in FXS includes debilitating hypersensitivity and reduced habituation to sensory inputs, particularly in the auditory domain (Castrén et al. 2003; Schneider et al. 2013; Ethridge et al. 2016). These symptoms are seen early in development and may lead to cognitive deficits and delayed language.

Auditory hypersensitivity and cortical processing deficits are observed in humans with FXS and the mouse model of FXS, the *Fmr1* knockout (KO) mice (Chen and Toth 2001; Rojas et al. 2001; Nielsen et al. 2002; Castrén et al. 2003; Rotschafer and Razak 2013, 2014; Ethridge et al. 2016; Sinclair et al. 2017; Rais et al. 2018). Recent studies of electroencephalographic (EEG) recordings from humans and rodents show remarkably similar changes in cortical neural oscillations, including increased resting EEG gamma band power, which may underlie sensory hypersensitivity in FXS (Ethridge et al. 2016; Wang et al. 2017; Lovelace et al. 2018). FMRP is expressed at multiple levels and cell types of the auditory neuraxis, and auditory brainstem deficits are present in global *Fmr1* KO mice (Strumbos et al. 2010; Beebe et al. 2014; Wang et al. 2014; Rotschafer et al. 2015; Garcia-Pino et al. 2017). While EEG recordings show abnormal responses at the cortical level, their origin and cell type specificity are not known.

Our previous studies suggested a novel mechanism for auditory hypersensitivity in FXS. Impaired development of parvalbumin (PV)-expressing inhibitory interneurons may underlie abnormal auditory cortical processing in *Fmr1* KO mice *via* matrix metalloproteinase-9 (MMP-9)-dependent regulation of perineuronal nets (PNNs) (Wen et al. 2018a). FMRP negatively regulates MMP-9 translation in neurons (Dziembowska and Wlodarczyk 2012; Dziembowska et al. 2013; Janusz et al. 2013), and MMP-9 levels are elevated in the brain of *Fmr1* KO mice and FXS postmortem brain tissues (Bilousova et al. 2009; Gkogkas et al. 2014; Sidhu et al. 2014; Wen et al. 2018a). MMP-9 is secreted from a number of cell types, including astrocytes and neurons (Szklarczyk et al. 2002). MMP-9 can also mediate changes in synaptic functions by signaling through the PI3K/Akt/mTOR pathway (Sidhu et al. 2014), potentially through BDNF/trkB signaling by cleaving pro-BDNF (Hwang et al. 2005; Yang et al. 2009) or activating integrin receptors (Legate et al. 2009; Chen et al. 2010). PI3K/Akt/mTOR pathway is implicated in FXS symptoms (Klann and Dever 2004; Ronesi and Huber 2008; Sharma et al. 2010; Gross et al. 2011; Hoeffer et al. 2012; Enriquez-Barreto and Morales 2016; Sato 2016). Therefore, MMP-9 may contribute to the changes in cortical hyperexcitability of *Fmr1* KO mice by affecting both inhibitory and excitatory neurons. *In vitro* slice recordings showed increased cortical excitability in mouse somatosensory cortex with deletion of *Fmr1* only from excitatory neurons, suggesting that FMRP expression in excitatory cortical neurons is required for normal cortical activity (Hays et al. 2011).

One method to begin understanding the cell type and circuit-specific mechanisms underlying the phenotypes in a genetic disorder is to remove the gene from specific cell types and circuits. Therefore, the main goal of this study was to determine the neurobehavioral phenotypes following deletion of *Fmr1* from forebrain excitatory neurons. Our data show that the removal of FMRP from forebrain excitatory neurons is sufficient to elicit FXS-associated symptoms including enhanced MMP-9 activity, mTOR/Akt signaling and resting state neural oscillations, impaired PV/PNN expression, and hyperactive behaviors. Together, these data suggest novel mechanisms lead to sensory hypersensitivity in FXS and potentially other ASD.

Materials and Methods

Mice

C57Bl/6 *Fmr1* KO mice and their congenic controls were obtained from Jackson Laboratories. In order to delete FMRP specifically from forebrain excitatory neurons, we crossed male Cre^{Nex1} with female $Fmr1^{flox/flox}$ mice to produce male $Cre^{Nex1}/Fmr1^{flox/y}$ conditional KO (cKO) mice and their wild-type (WT) littermates, $Fmr1^{flox/y}$ mice. $Fmr1^{flox}$ mice were obtained from Dr David Nelson (Baylor College of Medicine, Houston, Texas; Mientjes et al. 2006). *Nex1(NeuroD6)*-Cre mice (Goebbels et al. 2006) were generated in Dr Klaus Nave's lab (Göttingen, Germany) and breeding pairs were obtained from Dr Joshua Sanes' lab (Harvard University). Separate groups of mice were used for EEG recordings, biochemical analysis, and behavior tests. All genotypes were confirmed by PCR analysis of genomic DNA isolated from mouse tails. Mice were maintained in an AAALAC accredited facility under 12-h light/dark cycle and fed standard mouse chow. All procedures were done according to the National Institutes of Health and Institutional Animal Care and Use Committee (IACUC) guidelines. All procedures were approved by IACUC. Food and water were provided to the mice ad libitum.

Methods Overview

Goebbels et al. (2006) reported that most of the Cre activity in the Nex-Cre mice was in neocortex and hippocampus and marked pyramidal neurons of the cortex without affecting inhibitory or glial cells. These mice are often used for generating forebrain excitatory neuron-specific deletion of specific genes (Ballester-Rosado et al. 2010; Kazdoba et al. 2012; Kerrisk et al. 2013). To confirm deletion of FMRP in forebrain excitatory neurons, we examined expression of FMRP in the auditory cortex in P60–70 mice using immunostaining. FMRP is also expressed in auditory thalamus and midbrain of WT mice. To ensure that FMRP is deleted specifically in the forebrain, we quantified expression of FMRP in the medial geniculate body and inferior colliculus, major nuclei of the lemniscal auditory thalamus and midbrain, respectively. We also compared the effects of forebrain excitatory neuron-specific *Fmr1* deletion to global *Fmr1* KO mice of the same age on PV/PNN expression in adult auditory cortex. This was necessary because our previous study only examined the developing brain (Wen et al. 2018a). This was followed by measurements of the effects of FMRP deletion from forebrain excitatory neurons on gelatinase activity and mTOR/Akt phosphorylation in the adult auditory cortex of both global *Fmr1* KO and $Cre^{Nex1}/Fmr1^{Flox/y}$ cKO mice. We also recorded EEG signals from awake, freely moving mice to determine the effects of FMRP deletion from forebrain excitatory neurons on neural

oscillations in the adult auditory cortex to compare with our previous study of these phenotypes in global *Fmr1* KO mice (Lovelace et al. 2018). Finally, we examined anxiety-like behaviors and hyperactivity in $Cre^{Nex1}/Fmr1^{Flox/y}$ cKO mice to compare with our previous study of these phenotypes in global *Fmr1* KO mice (Dansie et al. 2013).

Immunofluorescence

Age-matched adult (P60–70) male *Fmr1* KO and WT or $Cre^{Nex1}/Fmr1^{Flox/y}$ cKO and $Fmr1^{Flox/y}$ mice were euthanized with isoflurane and sodium pentobarbital and perfused transcardially first with cold phosphate-buffered saline (PBS, 0.1 M) to clear out the blood and then with 4% paraformaldehyde (PFA) in 0.1 M PBS for fixation. Brains were removed and postfixed for 2–4 h in 4% PFA. The 40- to 100-µm brain slices were obtained using a vibratome (5100mz Campden Instruments). Auditory cortex was identified using hippocampal and brain atlas landmarks (Franklin and Paxinos 2008). For each brain, an average of 5–6 brain slices containing auditory cortex, thalamus, or inferior colliculus was collected.

Detection of PV/PNN

Immunostaining in 100-µm brain slices containing auditory cortex was performed as previously described with minor modifications (Wen et al. 2018a). Briefly, brain slices were postfixed for an additional 2 h in 4% PFA in 0.1 M PBS and then washed three times in 0.1 M PBS for 10 min. Slices were then quenched with 50 mM ammonium chloride for 15 min and washed three times with PBS for 10 min. Next, brain tissues were permeabilized with 0.1% Triton X-100 in PBS and nonspecific staining was blocked with a 5% normal goat serum (NGS; Sigma, catalog # G9023–10 mL) and 1% bovine serum albumin (BSA; Fisher Scientific, catalog # 9048468) in 0.1 M PBS solution. Brain slices were treated overnight with mouse anti-PV antibody (1:1000; Sigma, catalog # P3088, RRID:AB_477 329) to label parvalbumin(PV)-positive inhibitory interneurons. *Wisteria floribunda* agglutinin (WFA; 4 µg/mL; Vector Laboratories, catalog # FL-1351, RRID:AB_2 336875) in 0.1 M PBS containing 1% NGS, 0.5% BSA, and 0.1% Tween-20 solution was used to stain for PNNs containing aggrecan, known as WFA+ PNNs. WFA is a lectin, which binds glycosaminoglycan side chains of chondroitin sulfate proteoglycan (CSPG) aggrecan that is found in PNNs (Pizzorusso et al. 2002). After incubation, brain slices were washed three times in 0.1 M PBS containing 0.5% Tween-20 for 10 min and incubated with secondary antibody, donkey anti-mouse Alexa 594 (4 µg/mL, Thermo Fisher Scientific, catalog # A-21203, RRID:AB_2 535 789) in 0.1 M PBS for 1 h. Slices were then washed three times with 0.1 M PBS containing 0.5% Tween-20 for 10 min, mounted with Vectashield containing DAPI (Vector Labs, catalog # H-1200, RRID: AB_2336790) and Cytoseal (ThermoScientific, catalog # 8310–16).

Detection of FMRP Expression

Immunostaining for FMRP was performed using antigen retrieval methods, as previously described (Gabel et al. 2004; Christie et al. 2009; Gross et al. 2011), with the following modifications. The 40-µm brain slices were mounted onto Superfrost Plus Microscope Charged Slides (Fisher Scientific, catalog # 22–034-979), washed 3 times with TBS (0.1 M Tris-Cl pH 7.5, 0.15 M NaCl) for 10 min, treated with 0.8% Na Borohydride (Sigma S-9125) to reduce background and autofluorescence, and boiled in 0.01 M Na Citrate (Citric acid, sodium salt in water pH 6.0, Sigma C-8532) to achieve antigen retrieval. Permeabilization was performed with 0.5% Triton-X 100 for 20 min, and slices were stained overnight with mouse anti-FMRP (1:100; Developmental Studies Hybridoma Bank, catalog # 2F5-1-s, RRID: AB_10805421) and rabbit anti-NeuN (1:1000; Abcam, catalog # ab104225, RRID: AB_10711153) in TBS containing 2% normal donkey serum (NDS) and 0.1% Triton-X 100. After incubation with primary antibodies, slices were washed three times in TBS for 10 min and incubated with secondary antibodies for 1 h. Secondary antibodies used were donkey anti-rabbit Alexa 594 (4 µg/mL; Thermo Fisher Scientific, catalog # A-21207, RRID:AB_141637) and donkey anti-mouse Alexa 488 (4 µg/mL; Molecular Probes, catalog # A-21202, RRID:AB_141607). Slices were mounted with Vectashield containing DAPI and cytoseal and imaged.

Image Analysis

Slices were imaged using confocal microscopy (Leica SP5) by collecting a series of 20 high-resolution optical sections (1024 × 1024-pixel format) at 1-µm step interval (z-stack) that were captured for each slice using a ×10, ×20, or a ×63 water immersion objective (1.2 numerical aperture), with ×1 or ×5 zoom. All images were acquired under identical conditions. Each z-stack was collapsed into a single image by projection, converted to a TIFF file, encoded for blind analysis, and analyzed using ImageJ. ImageJ was used to identify and manually count PV-positive cells, WFA-positive PNN cells, PV/PNN colocalization, NeuN-positive cells, and FMRP/NeuN colocalization. Cortical layers were identified as previously reported (Anderson et al. 2009) and used for layer-specific analysis. Three slices were used per animal and cell counts were obtained in layers 1–4 of both the right and left auditory cortex (cell density was measured per layer). The freehand selection tool and measure function were used to specify layers of the auditory cortex and the point tool was used to label PNNs, PV cells, and NeuN cells added to the ROI manager. Particle Analysis Cell Counter plugin in Image J was used to count colocalization. Average cell density was calculated for each animal. Because we were comparing different mouse lines, the global *Fmr1* KO and the $Cre^{Nex1}/Fmr1^{Flox/y}$ cKO mice were evaluated against their specific controls (WT and $Fmr1^{Flox/y}$, respectively), and statistical analysis was performed with unpaired *t*-test using GraphPad Prism 6 software (RRID: SCR_002798). Data represent mean ± standard error of the mean (SEM).

Dye-Quenched Gelatin Assay and Analysis

The dye-quenched (DQ) gelatin plate assay was used to assess gelatinase activity. A FITC-quenched gelatin peptide that fluoresces following cleavage by gelatinases MMP-2 and MMP-9 was used to measure gelatinase proteolytic activity. Adult (P60–70) male WT and *Fmr1* KO mice or $Fmr1^{Flox/y}$ and $Cre^{Nex1}/Fmr1^{Flox/y}$ cKO litter mates (n = 4–6 mice per group) were euthanized with isoflurane, and the auditory cortex was dissected based on coordinates (Franklin and Paxinos 2008) and previous electrophysiological and dye-placement studies (Martin del Campo et al. 2012). Auditory cortex tissues were resuspended in lysis buffer (50 mM Tris-HCl, pH 7.4, 150 mM NaCl, 5 mM EDTA, 0.05% Triton X-100, and 1 mM PMSF) containing protease inhibitor cocktail (Sigma, catalog # P8340) and phosphatase inhibitor cocktail (Sigma, catalog # P0044). Lysates were measured for total protein concentrations using the protocol for the BCA colorimetric protein assay (Pierce, catalog # 23235).

Lysates were diluted in reaction buffer and mixed with a fluorescence-labeled gelatin substrate (Molecular Probes, E12055). Samples were incubated in the dark for 3 h at room temperature. The fluorescence intensity was analyzed using 495-nm excitation wavelength and 515-nm emission wavelength. The signal was measured every 20 min during the 3-h incubation period using a fluorescence microplate reader equipped with standard fluorescein filters (SoftMax Pro). For each time point, background fluorescence intensity was corrected by subtracting the values derived from reaction buffer control. A standard curve to assess gelatinase activity was generated using recombinant mouse MMP-9 (rmMMP-9, approximately 1500 pmol/min/µg, R&D Systems, catalog # 909-MM-010). A linear regression of rmMMP-9 activity (standard curve) and relative gelatinase activity based on the average fluorescence intensity of five replicates was used to assess gelatinase proteolytic activity in the brain samples. Statistical analysis was performed comparing KO samples to their corresponding WT samples with unpaired *t*-test using GraphPad Prism 6 software (RRID: SCR_002798). Data represent mean ± SEM.

Western Blot Analysis

The auditory cortex was removed from each mouse ($n = 4$ mice per group), cooled in PBS, and homogenized in ice-cold lysis buffer (50 mM Tris-HCl, pH 7.4, 150 mM NaCl, 5 mM EDTA, 0.05% Triton X-100, and 1 mM PMSF) containing protease inhibitor cocktail (Sigma, catalog # P8340) and phosphatase inhibitor cocktail (Sigma, catalog # P0044). The samples were rotated at 4°C for at least 1 h to allow for complete cell lysis and then cleared by centrifugation at 13200 rpm for 15 min at 4°C. Supernatants were isolated and boiled in reducing sample buffer (Laemmli 2× concentrate, S3401, Sigma) and separated on 8–16% Tris-Glycine SDS-PAGE precast gels (EC6045BOX, Life Technologies). Proteins were transferred onto Protran BA 85 Nitrocellulose membrane (GE Healthcare) and blocked for 1 h at room temperature in 5% skim milk (catalog # 170–6404, Bio-Rad). Primary antibody incubations were performed overnight at 4°C with antibodies diluted in TBS/0.1% Tween-20/5% BSA. The following primary antibodies were used: rabbit anti-mammalian target of rapamycin (mTOR; 7C10; catalog # 2983, RRID:AB_2105622), rabbit anti-phospho-mTOR (Ser2481; catalog # 2974, RRID:AB_2231885), rabbit anti-Akt (catalog # 9272; RRID:AB_10699016), rabbit anti-phospho-Akt (Ser473; catalog # 9271, RRID: AB_329825), mouse anti-Aggrecan at 1:200 (Novus, catalog # NB110–6852, RRID: AB_787911), mouse anti-PV (Millipore, catalog # MAB1572, RRID: AB_2174013), and rabbit anti-βactin at 1:2000 (Abcam, catalog # ab8227, RRID: AB_2305186). All primary antibodies were from Cell Signaling Technology and used at a dilution of 1:1000, unless stated otherwise.

Blots were washed 3 × 10 min with TBS/0.1% Tween-20 and incubated with the appropriate HRP-conjugated secondary antibodies for 1 h at room temperature in a TBS/0.1% Tween-20/5% BSA solution. The secondary antibodies used were HRP-conjugated donkey anti-mouse IgG (Jackson ImmunoResearch, catalog # 715-035-150, RRID: AB_2340770) or HRP-conjugated goat anti-rabbit IgG (Jackson ImmunoResearch, catalog # 111-035-003, RRID: AB_2313567). After secondary antibody incubations, blots were washed 3 × 10 min in TBS/0.1% Tween-20 and incubated in ECL 2 Western Blotting Substrate (Thermo Scientific, catalog # 80196) and a signal was collected with CL-XPosure film (Thermo Scientific, catalog # 34090). For re-probing, membrane blots were washed in stripping buffer (2% SDS, 100 mM β-mercaptoethanol, 50 mM Tris-HCl, pH 6.8) for 30 min at 55°C, then rinsed repeatedly with TBS/0.1% Tween-20, finally blocked with 5% skim milk, and then re-probed. Developed films were then scanned, and band density was analyzed by measuring band and background intensity using Adobe Photoshop CS5.1 software (RRID:SCR_014199). Four samples per group (WT vs. *Fmr1* KO or $Fmr1^{Flox/y}$ vs. $Cre^{Nex1}/Fmr1^{Flox/y}$ cKO) were run per blot, and precision/tolerance (P/T) ratios for *Fmr1* KO and $Cre^{Nex1}/Fmr1^{Flox/y}$ cKO samples were normalized to averaged P/T ratios of WT and $Fmr1^{Flox/y}$ samples, respectively. Statistical analysis was performed with unpaired *t*-test using GraphPad Prism 6 software. Data represent mean ± SEM.

Surgery for In Vivo EEG Recordings

Male $Cre^{Nex1}/Fmr1^{Flox/y}$ cKO ($n = 9$) and their littermate controls, $Fmr1^{Flox/y}$ ($n = 9$) mice, were used for the EEG studies. Mice were anesthetized with isoflurane inhalation (0.2–0.5%) and an injection of ketamine and xylazine (i.p. 80/10 mg/kg), secured in a bite bar, and placed in a stereotaxic apparatus (model 930; Kopf). Artificial tear gel was applied to the eyes to prevent drying. Toe pinch reflex was used to measure anesthetic state every 10 min throughout the surgery, and supplemental doses of ketamine and xylazine were administered as needed. Once the mouse was anesthetized, a midline sagittal incision was made along the scalp to expose the skull. A Foredom dental drill was used to drill 1-mm-diameter holes in the skull overlying the right auditory cortex (−1.6 mm, +4.8 mm), left frontal lobe (+3.0 mm, −1.6 mm), and left occipital (−4.2 mm, −5.1 mm) (coordinate relative to Bregma: anterior/posterior, medial/lateral). Three channel electrode posts from Plastics One (MS333-2-A-SPC) were attached to 1 mm stainless steel screws from Plastics One (8L003905201F), and screws were advanced into drilled holes until secure. Special care was taken not to advance the screws beyond the point of contact with the Dura. Dental cement was applied around the screws, on the base of the post, and to the exposed skull. Triple antibiotic was applied along the edges of the dental cement followed by an injection of subcutaneous Buprenorphine (0.1 mg/kg). Mice were placed on a heating pad to aid recovery from anesthesia. A second Buprenorphine injection was administered between 6 and 10 h after surgery. Mice were then individually housed, returned to the vivarium, and monitored daily until the day of EEG recordings. The separation between the last postsurgical buprenorphine injection and EEG recordings was between 3 and 5 days.

Electrophysiology

Resting and auditory event-related potential (ERP) recordings were obtained using the BioPac system (BIOPAC Systems, Inc.) from awake and freely moving mice as published previously (Lovelace et al. 2018). Mice were allowed to habituate to the recording chamber for 15 min prior to being connected to the BioPac system. A three-channel tether was connected to the electrode post (implanted during surgery) under brief isoflurane anesthesia. The mouse was then placed inside a grounded Faraday cage after recovery from isoflurane. This tether was then connected to a commutator located directly above the cage. Mice were then allowed to habituate to being connected to the tether for an additional 15 min before EEG recordings were obtained.

The BioPac MP150 acquisition system was connected to two EEG 100C amplifier units (one for each channel) to which the

commutator was attached. The lead to the occipital cortex was used as reference for both frontal and auditory cortex screw electrodes. The acquisition hardware was set to high-pass (>0.5 Hz) and low-pass (<100 Hz) filters. Normal EEG output data were collected with gain maintained the same (10 000×) between all recordings. Data were sampled at a rate of either 2.5 or 5 kHz using Acqknowledge software and downsampled to 1024 Hz post hoc using Analyzer 2.1 (Brain Vision Inc.). Sound delivery was synchronized with EEG recording using a TTL pulse to mark the onset of each sound in a train. Resting EEGs were recorded for 5 min (no auditory stimuli were presented), followed by recordings in response to auditory stimulation. After these experiments were completed, mice were returned to the colony and euthanized on a later date.

Acoustic Stimulation

All experiments were conducted in a sound-attenuated chamber lined with anechoic foam (Gretch-Ken Industries, Oregon). Acoustic stimuli were generated using RVPDX software and RZ6 hardware (Tucker-Davis Technologies) and presented through a free-field speaker (MF1 Multi-Field Magnetic Speaker; Tucker-Davis Technologies) located 12 inches directly above the cage. Sound pressure level (SPL) was modified using programmable attenuators in the RZ6 system. The speaker output was ~70 dB SPL at the floor of the recording chamber with fluctuation of ±3 dB for frequencies between 5 and 35 kHz as measured with a ¼ inch Bruel & Kjaer microphone.

We used acoustic stimulation paradigms that have been previously established in *Fmr1* KO mice (Lovelace et al. 2018), which is analogous to work in humans with FXS (Ethridge et al. 2017). A chirp-modulated signal (henceforth, "chirp") to induce synchronized oscillations in EEG recordings was used. The chirp is a 2-s broadband noise stimulus with amplitude modulated (100% modulation depth) by a sinusoid whose frequencies increase (up-chirp) or decrease (down-chirp) linearly in the 1–100 Hz range (Artieda et al. 2004; Purcell et al. 2004; Pérez-Alcázar et al. 2008). The chirp facilitates a rapid measurement of transient oscillatory response (delta to gamma frequency range) to auditory stimuli of varying frequencies and can be used to compare oscillatory responses in different groups in clinical and pre-clinical settings (e.g., Purcell et al. 2004). Inter-trial coherence analysis (Tallon-Baudry et al. 1996) can then be used to determine the ability of the neural generator to synchronize oscillations to the frequencies present in the stimulus.

To avoid onset responses contaminating phase locking to the amplitude modulation of the chirp, the stimulus was ramped in sound level from 0% to 100% over 1 s (rise time), which then smoothly transitioned into chirp modulation of the noise. Up- and down-chirp trains were presented 300 times each (for a total of 600 trains). Both directions of modulation were tested to ensure any frequency-specific effects were not due to the frequency transition history within the stimulus. Up- and down-chirp trains were presented in an alternating sequence. The interval between each train was randomly varied between 1 and 1.5 s.

To study evoked response amplitudes and habituation, trains of 100 ms broadband noise were presented at two repetition rates, 0.25 Hz (a nonhabituating rate) and 4 Hz (a strongly habituating rate) (Lovelace et al. 2016). Each train consisted of 10 noise bursts and the inter-train interval used was 8 s. Each repetition rate was presented 100 times in an alternating pattern (0.25, 4, 0.25, 4 Hz, etc.). The onset of trains and individual noise bursts were tracked with separate TTL pulses that were used to quantify latency of response.

Data Analysis

Data were extracted from Acqknowledge and files saved in a file format (EDF) compatible with BrainVision Analyzer 2.1 software. All data were notch filtered at 60 Hz to remove residual line frequency power from recordings. EEG artifacts were removed using a semiautomatic procedure in Analyzer 2.1 for all recordings. Less than 20% of data were rejected due to artifacts from any single mouse. Resting EEG data were divided into 1-s segments, and fast Fourier transforms (FFT) were calculated on each segment using 0.5-Hz bins and then average power (μV^2/Hz) was calculated for each mouse from 1 to 100 Hz. Power was then further binned into standard frequency bands: delta (1–4 Hz), theta (4–10 Hz), alpha (10–13 Hz), beta (13–30 Hz), low gamma (30–55 Hz), and high gamma (65–100 Hz). Responses to chirp trains were analyzed using Morlet wavelet analysis. Chirp trains were segmented into windows of 500 ms before chirp onset to 500 ms after the end of the chirp sound (total of 3 s because each chirp was 2 s in duration). EEG traces were processed with Morlet wavelets from 1 to 100 Hz using complex number output (voltage density, μV/Hz) for inter trial phase coherence (ITPC) calculations and power density (μV^2/Hz) for non–phase-locked single-trial power (STP) calculations and baseline corrected non–phase-locked STP (induced power). Wavelets were run with a Morlet parameter of 10 as this gave the best frequency/power discrimination. This parameter was chosen since studies in humans found most robust difference around 40 Hz, where this parameter is centered (Ethridge et al. 2017). To measure phase synchronization at each frequency across trials, ITPC was calculated. The equation used to calculate ITPC is

$$ITPC(f,t) = \frac{1}{n}\sum_{k=1}^{n}\frac{F_k(f,t)}{|F_k(f,t)|},$$

where f is the frequency, t is the time point, and k is the trial number. Thus, $F_k(f,t)$ refers to the complex wavelet coefficient at a given frequency and time for the kth trial. There were no less than 275 trials (out of 300) for any given mouse after segments containing artifacts were rejected.

Statistical Analysis and Definition of Movement States

Statistical group comparisons of chirp responses (ITPC and STP) and broadband noise trains (ITPC and induced power) were quantified by wavelet analysis. Analysis was conducted by binning time into 256 parts and frequency into 100 parts, resulting in a 100×256 matrix. Nonparametric cluster analysis was used to determine contiguous regions in the matrix that were significantly different from a distribution of 2000 randomized Monte Carlo permutations based on previously published methods (Maris and Oostenveld 2007). Briefly, if the cluster sizes of the real genotype assignments (both positive and negative direction, resulting in a two-tailed alpha of $P = 0.025$) were larger than 97.25% of the random group assignments, those clusters were considered significantly different between genotypes. This method avoids statistical assumptions about the data and corrects for multiple comparisons.

Because movement can alter cortical gain (Niell and Stryker 2010; Fu et al. 2015) and *Fmr1* KO mice show hyperactivity, a piezoelectric transducer was placed underneath the recording cage to detect when the mouse was moving. The term "resting"

is used to indicate EEGs recorded in these mice without any specific auditory stimuli. The term "still" is used to describe resting EEG when the mouse was stationary. The term "moving" is used to describe resting EEG when the mouse was moving based on a threshold criterion for the piezoelectric signal that was confirmed by analyzing the video recording (under IR light) that was taken throughout the EEG recording procedure. In all cases where genotype means are reported, SEM was used. The genotype differences in resting power were analyzed on six dependent variables using one-way multivariate analysis of covariance (MANCOVA) with one covariate (movement), independent variables (IV): Genotype (*Fmr1*$^{Flox/y}$ *control*, *Cre*^{Nex1}/*Fmr1*$^{Flox/y}$ cKO mice) and dependent variables (DV): 6 frequency bins (delta to high gamma). The proportion of time spent moving during the 5-min recording session was used as a covariate to isolate the effects of genotype and control for the effect movement has on cortical gain. When multiple comparisons for MANCOVA were made, genotype comparisons were corrected using Bonferroni adjustments. The divisor for Bonferroni correction for multiple comparisons (for six frequency bands) on MANCOVA was set to 6, $\alpha = 0.05/6 = 0.0083$. Data are often expressed and plotted as ratio of control group values to gauge relative differences in various factors using the same scale.

Behavioral Assessments

Open-Field Test

Anxiety was tested in P60 mice (6 mice per group) by quantifying their tendency to travel to the center of an open field and time spent in thigmotaxis (Yan et al. 2004, 2005). A 72 × 72-cm open-field (OF) arena with 50-cm-high walls was constructed from opaque acrylic sheets with a clear acrylic sheet for the bottom The OF arena was placed in a brightly lit room, and one mouse at a time was placed in a corner of the open field and allowed to explore for 10 min while being recorded with digital video from above. The floor was cleaned with 2–3% acetic acid, 70% ethanol, and water between tests to eliminate odor trails. The mice were tested between the hours of 9:00 AM and 1:00 PM, and this test was always performed prior to the elevated plus maze. The arena was subdivided into a 4 × 4 grid of squares with the middle of the grid defined as the center. A line 4 cm from each wall was added to measure thigmotaxis. Locomotor activity was scored by the analysis of total line crosses and speed as described previously with some modifications (Brown et al. 1999; Yan et al. 2005) using TopScan Lite software (Clever Sys., Inc., Reston). A tendency to travel to the center (total number of entries into large and small center squares) and the time in thigmotaxis were used as an indicator of anxiety using TopScan Lite software (CleverSys Inc). The analysis was performed in 5-min interval for the total 10-min exploration duration. Assessments of the digital recordings were performed blind to the condition. Statistical analysis was performed with unpaired *t*-test using GraphPad Prism 6 software. Data represent mean ± SEM.

Elevated Plus Maze

The elevated plus maze consisted of 4 arms in a plus configuration. Two opposing arms had 15-cm tall walls (closed arms) and two arms were without walls (open arms). The entire maze sat on a stand 1 m above the floor. Each arm measured 30 cm long and 10 cm wide. Mice were allowed to explore the maze for 10 min while being recorded by digital video from above. The maze was wiped with 2–3% acetic acid, 70% ethanol, and water between each test to eliminate odor trails. This test was always done following the OF test. TopScan Lite software was used to measure the percent of time spent in open arms and speed. The time spent in open arm was used to evaluate anxiety-like behavior (Carobrez and Bertoglio 2005). The speed and total arm entries were measured to evaluate overall locomotor activity. The analysis was performed in 5-min interval for the total 10 min exploration duration. Assessments of the digital recordings were done blind to the condition using TopScan Lite software. Statistical analysis was performed with unpaired *t*-test using GraphPad Prism 6 software. Data represent mean ± SEM.

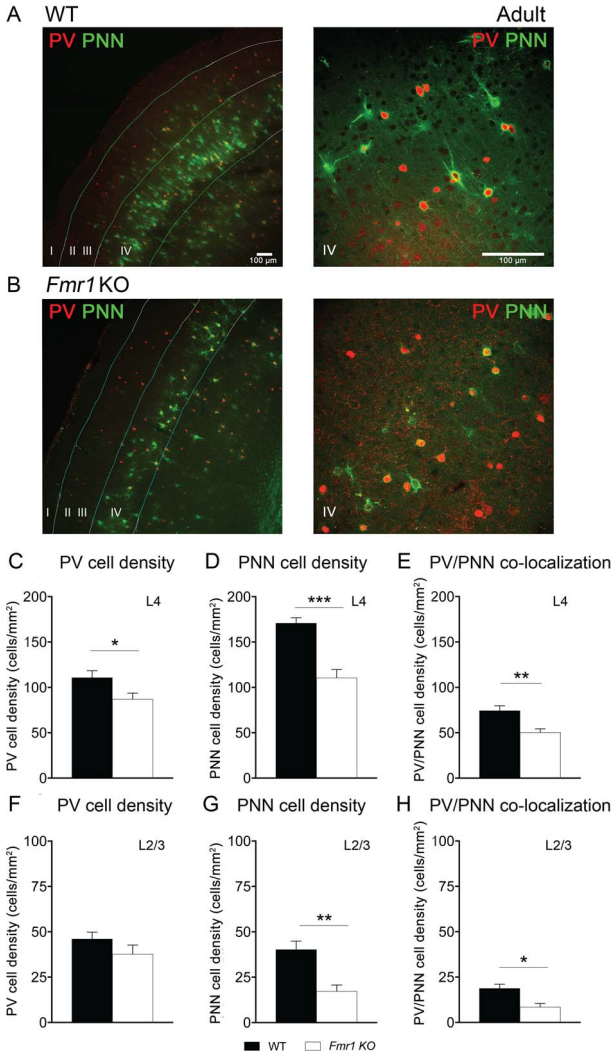

Figure 1. Impaired WFA+ PNNs and PV/PNN colocalization are detected in the auditory cortex of adult *Fmr1* KO mice. (*A*,*B*) Confocal images showing PV immunoreactivity (red) and WFA-positive PNN labeling (green) in the auditory cortex of adult WT (*A*) and *Fmr1* KO mice (*B*). (*C*–*H*) Quantitative analysis of the density of PV, PNN, or PV/PNN-positive cells. Graphs show mean ± SEM ($n = 6$/group, $^{*}P < 0.05$; $^{**}P < 0.01$; $^{***}P < 0.001$, *t*-test). PV cell density was significantly reduced in L4 auditory cortex of *Fmr1* KO mice compared with WT. (*C*) No significant changes were observed in PV cell density in L2–3 between the WT and *Fmr1* KO mice (*F*). PNN cell density was significantly reduced in L4 (*D*) and L2–3 (*G*) auditory cortex of *Fmr1* KO mice compared with WT mice (note that only WFA+ cells were counted to measure PNN density). PV/PNN colocalization was also significantly reduced in L4 (*E*) and L2–3 (*H*) auditory cortex of *Fmr1* KO mice.

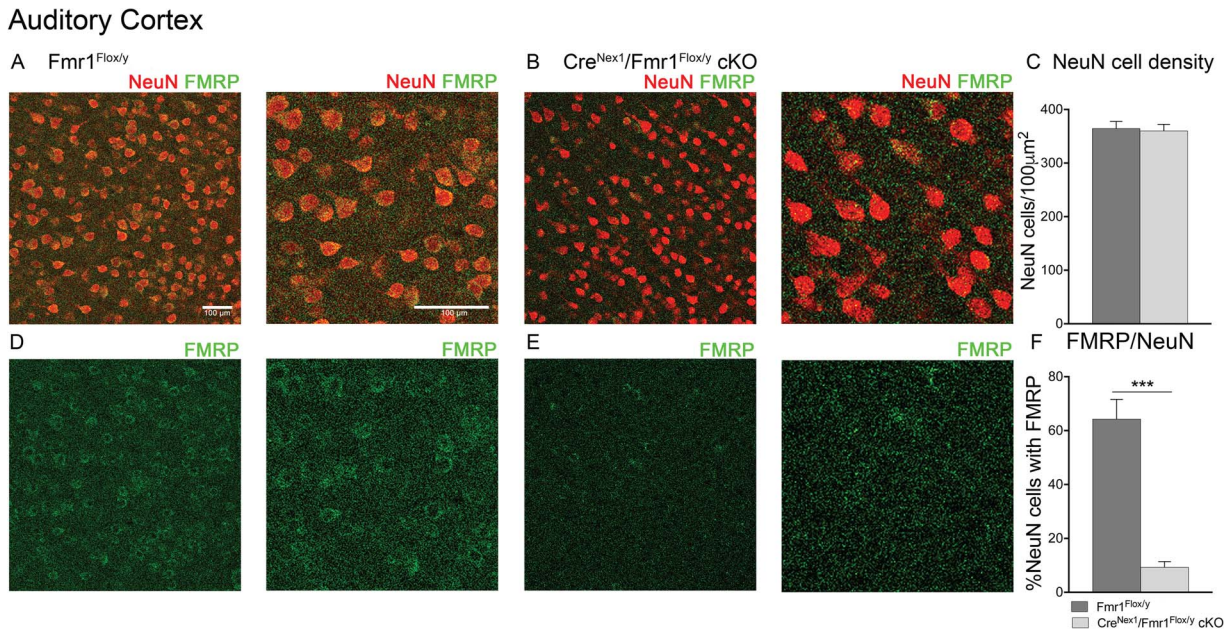

Figure 2. Excitatory-specific FMRP loss was observed in the auditory cortex of adult $Cre^{Nex1}/Fmr1^{Flox/y}$ cKO mice. (*A*,*B*) Confocal images showing NeuN (red) and FMRP (green) immunoreactivity in the auditory cortex of adult $Fmr1^{Flox/y}$ and $Cre^{Nex1}/Fmr1^{Flox/y}$ cKO mice. (*C*) Quantitative analysis of the density of NeuN-positive cells. Graphs show mean ± SEM. No significant changes were observed in NeuN cell density in the $Fmr1^{Flox/y}$ and $Cre^{Nex1}/Fmr1^{Flox/y}$ cKO mice. (*D*,*E*) Confocal images showing FMRP (green) immunoreactivity in the auditory cortex of adult $Fmr1^{Flox/y}$ and $Cre^{Nex1}/Fmr1^{Flox/y}$ cKO mice. (*F*) Quantitative analysis of the percentage of FMRP-positive NeuN cells. Graphs show mean ± SEM ($n = 3$/group, $^{***}P < 0.001$, *t*-test). There is a significant decrease in the percentage of NeuN+ neurons with FMRP in the $Cre^{Nex1}/Fmr1^{Flox/y}$ cKO mice compared with $Fmr1^{Flox/y}$ mice.

Results

In the current study, we examined 1) whether the deficits in PV and PNN expression observed in developing auditory cortex of global *Fmr1* KO mice are also seen in adulthood; 2) the effects of FMRP deletion from forebrain excitatory neurons on gelatinase activity, PV/PNN expression, and mTOR/Akt phosphorylation in the adult auditory cortex of $Cre^{Nex1}/Fmr1^{Flox/y}$ cKO mice; and 3) whether FMRP deletion from forebrain excitatory neurons affects neural oscillations in the auditory cortex of $Cre^{Nex1}/Fmr1^{Flox/y}$ cKO mice, including resting gamma power and evoked gamma synchronization, and elicits abnormal FXS-associated behaviors, such as hyperactivity and anxiety.

Reduced PNNs and PV/PNN Colocalization Were Observed in the Auditory Cortex of Adult Global Fmr1 KO Mice

We recently showed evidence for abnormal development of PV neurons and PNNs in the developing auditory cortex of global *Fmr1* KO mice (Wen et al. 2018a). Here, we examined whether the deficits were also seen in the adult auditory cortex of *Fmr1* KO mice. For this, we characterized the density of PV+ cells and fluorescently tagged WFA was used to assess the density of WFA+ PNN-containing cells in L1–4 of adult WT and *Fmr1* KO auditory cortex (Fig. 1A–H). Statistical analysis using unpaired *t*-test revealed that there was a significant reduction in PV cell density in L4 of *Fmr1* KO auditory cortex compared with WT ($n = 6$, $t(10) = 2.37$, $P = 0.0391$, *t*-test) (Table 2 and Fig. 1C). However, no significant changes were observed in PV cell density in L2/3 of *Fmr1* KO auditory cortex compared with WT ($n = 6$, $P = 0.230$, *t*-test) (Table 2 and Fig. 1F). We observed a significant reduction in WFA+ PNN cell density in *Fmr1* KO auditory cortex compared with WT in both L4 ($n = 6$, $t(10) = 5.50$, $P = 0.0003$, *t*-test) and L2/3 ($n = 6$, $t(10) = 4.02$, $P = 0.007$, *t*-test) (Table 2 and Fig. 1D,G). We also analyzed the density of PV/PNN double-labeled cells and found that formation of WFA+ PNNs was impaired around PV cells in adult *Fmr1* KO auditory cortex compared with WT in both L4 ($n = 6$, $t(10) = 3.61$, $P = 0.0048$, *t*-test) and L2/3 ($n = 6$, $t(10) = 3.37$, $P = 0.0151$, *t*-test) (Table 2 and Fig. 1E,H). Taken together, these data demonstrate that similar to what we observed in the developing *Fmr1* KO mice, formation of WFA+ PNNs and PV/PNN colocalization remains impaired in the adult auditory cortex of global *Fmr1* KO mice. These deficits may underlie the enhanced sound driven response in adult global *Fmr1* KO auditory cortex (Rotschafer and Razak 2013).

FMRP Immunoreactivity Was Significantly Reduced in Excitatory Neurons of Auditory Cortex of Adult $Cre^{Nex1}/Fmr1^{Flox/y}$ cKO Mice

To achieve the deletion of FMRP from forebrain excitatory neurons, we crossed male Cre^{Nex1} with female $Fmr1^{flox/flox}$ KO mice and analyzed the expression of FMRP within the regions of the auditory pathway in the $Cre^{Nex1}/Fmr1^{Flox/y}$ cKO and their littermate controls, $Fmr1^{Flox/y}$ mice (Fig. 2, Supplementary Fig. 1). $Fmr1^{Flox/y}$ mice showed FMRP expression in NeuN+ cells (Fig. 2A,D) in the auditory cortex. FMRP immunoreactivity was visibly reduced in the cortex of adult $Cre^{Nex1}/Fmr1^{Flox/y}$ cKO mice (Fig. 2B,E). No significant changes were observed in NeuN cell density in the $Fmr1^{Flox/y}$ and $Cre^{Nex1}/Fmr1^{Flox/y}$ cKO mice ($n = 3$, $P = 0.695$, *t*-test) (Table 2 and Fig. 2C). However, there was a significant decrease in the percentage of NeuN+ neurons with FMRP in the $Cre^{Nex1}/Fmr1^{Flox/y}$ cKO mice compared with $Fmr1^{Flox/y}$ mice ($n = 3$, $t(4) = 12.6$, $P = 0.0002$, *t*-test) (Table 1 and Fig. 2F). The remaining NeuN+ cells with FMRP are presumed to be GABAergic neurons (Tamamaki et al. 2003). These data confirm

Table 1 Summary table showing percentage of NeuN+ neurons with FMRP expression in different regions of the auditory pathway in the *Fmr1*$^{Flox/y}$ and *Cre*^{Nex1}/*Fmr1*$^{Flox/y}$ cKO mice (mean ± SEM)

	Fmr1 $^{Flox/y}$	Cre^{Nex1}/*Fmr1*$^{Flox/y}$ cKO
Auditory cortex	64 ± 4	9 ± 1*** (p = 0.0002)
Central inferior colliculus	59 ± 2	53 ± 1
External inferior colliculus	54 ± 4	50 ± 3
Medial geniculate body	67 ± 3	69 ± 3

Statistical analysis of differences between Cre^{Nex1}/*Fmr1*$^{Flox/y}$ cKO mice and their WT counterparts was performed using *t*-test (unpaired, two-tailed): ***$P < 0.001$.

that FMRP was deleted from forebrain excitatory neurons in the auditory cortex.

Unlike the auditory cortex, no significant changes in FMRP expression were observed in the inferior colliculus and the auditory thalamus (medial geniculate body; Supplementary Fig. 1). FMRP expression was detected in NeuN+ neurons in the central (Supplementary Fig. 1A,B) and external inferior colliculus (Supplementary Fig. 1D,E) and medial geniculate body (Supplementary Fig. 1G,H) of *Cre*^{Nex1}/*Fmr1*$^{Flox/y}$ cKO mice. No significant changes were observed in the percentage of NeuN+ neurons showing FMRP immunoreactivity in the central ($n = 3$, $P = 0.0971$, *t*-test; Table 1 and Supplementary Fig. 1C) or external inferior colliculus ($n = 3$, $P = 0.0718$, *t*-test; Table 1 and Supplementary Fig. 1F) of *Cre*^{Nex1}/*Fmr1*$^{Flox/y}$ cKO mice compared with *Fmr1*$^{Flox/y}$ mice. In the medial geniculate body as well, no significant changes in the percentage of NeuN+ neurons with FMRP were found between the *Fmr1*$^{Flox/y}$ and *Cre*^{Nex1}/*Fmr1*$^{Flox/y}$ cKO mice ($n = 3$, $P = 0.697$, *t*-test; Table 1 and Supplementary Fig. 1I). These data confirm a significant loss of FMRP from excitatory neurons in the auditory cortex, but not inferior colliculus or medial geniculate body, of *Cre*^{Nex1}/*Fmr1*$^{Flox/y}$ cKO mice.

Deletion of FMRP from Excitatory Neurons Reduces PV, PNN, and PV/PNN Colocalization in the Auditory Cortex of Adult *Cre*^{Nex1}/*Fmr1*$^{Flox/y}$ cKO Mice

We examined PV+ and WFA+ PNN-containing cell density in auditory cortex of adult *Fmr1*$^{Flox/y}$ and *Cre*^{Nex1}/*Fmr1*$^{Flox/y}$ cKO mice (Fig. 3A–H). Similar to the adult *Fmr1* KO mice, there was a significant decrease in PV cell density in auditory cortex of *Cre*^{Nex1}/*Fmr1*$^{Flox/y}$ cKO mice compared with their littermate controls, *Fmr1*$^{Flox/y}$ mice in both L4 ($n = 6$, $t(10) = 2.53$, $P = 0.0298$, *t*-test) and L2/3 ($n = 6$, $t(10) = 2.47$, $P = 0.0483$, *t*-test) (Table 2 and Fig 3C,F). WFA+ PNN cell density was also significantly reduced in auditory cortex of *Cre*^{Nex1}/*Fmr1*$^{Flox/y}$ cKO mice compared with *Fmr1*$^{Flox/y}$ in both L4 ($n = 6$, $t(10) = 10.3$, $P < 0.0001$, *t*-test) and L2/3 ($n = 6$, $t(10) = 7.77$, $P = 0.0002$, *t*-test) (Table 2 and Fig. 3D,G). In addition, PV/PNN colocalization was significantly decreased in auditory cortex of *Cre*^{Nex1}/*Fmr1*$^{Flox/y}$ cKO mice compared with *Fmr1*$^{Flox/y}$ in L4 ($n = 6$, $t(10) = 5.12$, $P = 0.0005$, *t*-test) and L2/3 ($n = 6$, $t(10) = 7.19$, $P = 0.0004$, *t*-test) (Table 2 and Fig. 3E,H). These data indicate that the removal of FMRP from excitatory neurons is sufficient to trigger abnormal development of WFA+ PNNs in the auditory cortex, specifically around inhibitory PV interneurons. Thus, a cell type-specific loss of FMRP may lead to a network-level dysfunction.

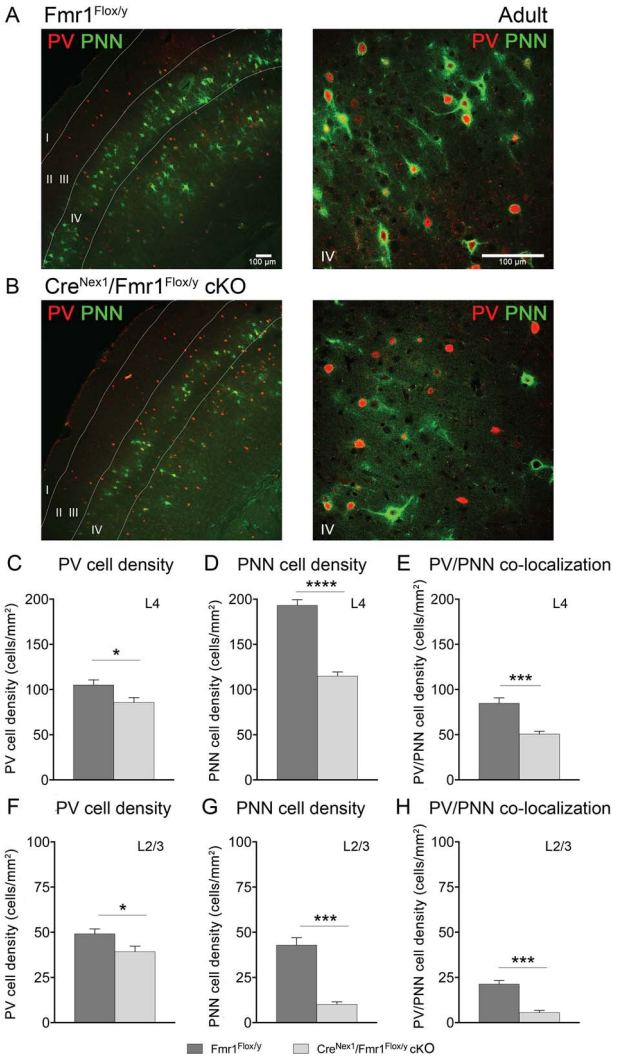

Figure 3. Deletion of *Fmr1* from excitatory neurons affected development of WFA+ PNNs and PV/PNN colocalization in the adult mouse auditory cortex. (*A*,*B*) Confocal images showing PV immunoreactivity (red) and WFA-positive PNN labeling (green) in the auditory cortex of adult *Fmr1*$^{Flox/y}$ (A) and *Cre*^{Nex1}/*Fmr1*$^{Flox/y}$ cKO (B) mice. (*C*–*H*) Quantitative analysis of the density of PV, PNN, or PV/PNN-positive cells. Graphs show mean ± SEM ($n = 6$/group, *$P < 0.05$; ***$P < 0.001$; ****$P < 0.0001$, *t*-test). PV cell density was significantly reduced in L4 (*C*) and L2–3 (*F*) auditory cortex of *Cre*^{Nex1}/*Fmr1*$^{Flox/y}$ cKO mice compared with *Fmr1*$^{Flox/y}$. PNN cell density was significantly reduced in L4 (*D*) and L2–3 (*G*) auditory cortex of *Cre*^{Nex1}/*Fmr1*$^{Flox/y}$ cKO mice compared with *Fmr1*$^{Flox/y}$ (note that only WFA-positive cells were counted to measure PNN density). PV/PNN colocalization was also significantly reduced in L4 (E) and L2–3 (*H*) auditory cortex of *Cre*^{Nex1}/*Fmr1*$^{Flox/y}$ cKO mice compared to *Fmr1*$^{Flox/y}$.

Total Aggrecan Levels Are Reduced, While Cleaved Aggrecan Levels and Gelatinase Activity Are Enhanced in the Auditory Cortex of Adult *Cre*^{Nex1}/*Fmr1*$^{Flox/y}$ cKO Mice

As enhanced gelatinase activity may contribute to the loss of PNNs by cleaving extracellular matrix (ECM), we performed a gelatinase activity assay. A significant increase in gelatinase activity was observed in both *Fmr1* KO ($n = 4$, $t(6) = 4.26$, $P = 0.0053$, *t*-test) and *Cre*^{Nex1}/*Fmr1*$^{Flox/y}$ cKO mice ($n = 4$, $t(6) = 3.99$, $P = 0.0072$, *t*-test) as compared to their respective WT

Table 2 Summary table showing density of PV cells, WFA+ PNNs, and PV/PNN colocalization in the auditory cortex of adult WT, *Fmr1* KO, $Fmr1^{Flox/y}$, and $Cre^{Nex1}/Fmr1^{Flox/y}$ cKO mice (mean ± SEM)

	WT		*Fmr1* KO		$Fmr1^{Flox/y}$		$Cre^{Nex1}/Fmr1^{Flox/y}$ cKO	
	L4	L2/3	L4	L2/3	L4	L2/3	L4	L2/3
PV+ cell density	111 ± 7	46 ± 4	87 ± 6* ($P = 0.0391$)	38 ± 5	105 ± 5	49 ± 3	86 ± 5* ($P = 0.0298$)	39 ± 3* ($P = 0.0483$)
PNN+ cell density	171 ± 6	40 ± 5	111 ± 9*** ($P = 0.0003$)	17 ± 3** ($P = 0.007$)	193 ± 6	43 ± 4	115 ± 4**** ($P < 0.0001$)	10 ± 1*** ($P = 0.0002$)
PV+/PNN+ colocalization	74 ± 5	19 ± 2	51 ± 3** ($P = 0.0048$)	8 ± 2* ($P = 0.0151$)	85 ± 6	21 ± 2	51 ± 3*** ($P = 0.0005$)	6 ± 1*** ($P = 0.0004$)

Statistical analysis of differences between *Fmr1* KO and $Cre^{Nex1}/Fmr1^{Flox/y}$ cKO mice with their respective WT counterparts was performed using *t*-test (unpaired, two-tailed).
*$P < 0.05$, **$P < 0.01$, ***$P < 0.001$, ****$P < 0.0001$.

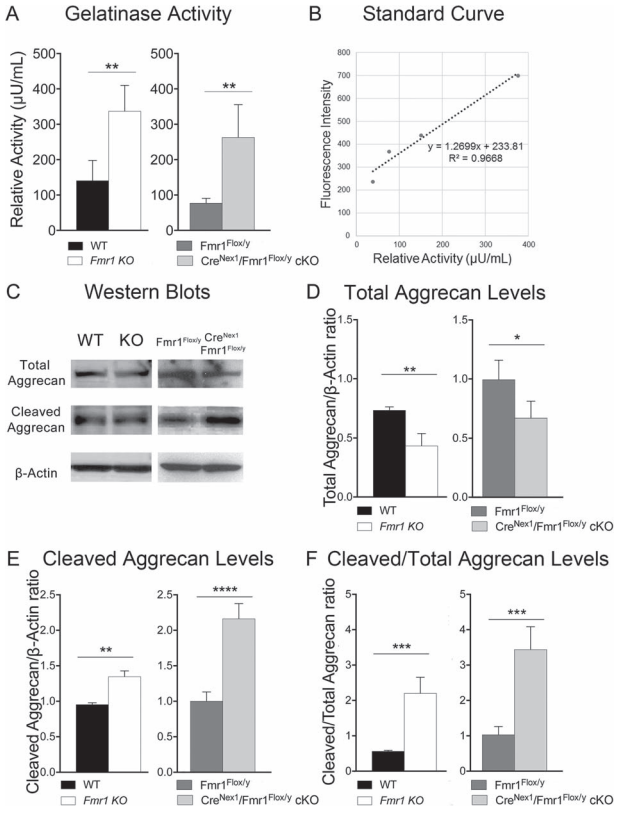

Figure 4. Total aggrecan levels are reduced, whereas cleaved aggrecan levels and gelatinase activity are elevated in the auditory cortex of adult excitatory neuron–specific $Cre^{Nex1}/Fmr1^{Flox/y}$ cKO mice. (*A*) Relative gelatinase activity in adult auditory cortex of WT, *Fmr1* KO, $Fmr1^{Flox/y}$, and $Cre^{Nex1}/Fmr1^{Flox/y}$ cKO mice. Graph shows mean ± SEM ($n = 4$/group, **$P < 0.01$, *t*-test). Gelatinase activity is elevated in *Fmr1* KO and $Cre^{Nex1}/Fmr1^{Flox/y}$ cKO mice as compared with WT and $Fmr1^{Flox/y}$ mice, respectively. (*B*) Standard curve showing gelatinase activity of recombinant MMP-9. Linear regression graph represents mean ± SEM ($n = 5$). (*C*) Western blots showing total and cleaved forms of aggrecan. (*D–F*) Graphs show mean ± SEM ($n = 4$/group; *$P < 0.05$, **$P < 0.01$, ***$P < 0.001$, ****$P < 0.0001$; *t*-test). Total aggrecan levels were significantly reduced in both the *Fmr1* KO and $Cre^{Nex1}/Fmr1^{Flox/y}$ cKO mice compared with WT and $Fmr1^{Flox/y}$ mice (*D*). In contrast, cleaved aggrecan levels were significantly increased in the auditory cortex of both *Fmr1* KO and $Cre^{Nex1}/Fmr1^{Flox/y}$ cKO mice compared with their WT counterparts (*E*). Cleaved aggrecan to total aggrecan ratio was significantly increased in both the *Fmr1* KO and $Cre^{Nex1}/Fmr1^{Flox/y}$ cKO mice compared with WT and $Fmr1^{Flox/y}$ mice, respectively (*F*).

counterparts, WT and $Fmr1^{Flox/y}$ mice (Fig. 4A). While the gelatinase activity assay measures both MMP-2 and MMP-9 proteolytic activity, our previous study showed that MMP-2 levels were similar in the adult auditory cortex of WT and *Fmr1* KO mice, while MMP-9 levels were significantly increased in the *Fmr1* KO mice (Lovelace et al. 2016). This suggests that the observed increase in gelatinase activity in adult *Fmr1* KO and $Cre^{Nex1}/Fmr1^{Flox/y}$ cKO mouse auditory cortex could be due to increased MMP-9 levels.

Enhanced gelatinase activity may result in excessive cleavage of aggrecan and a reduction in aggrecan-containing PNNs detected with WFA (Roughley and Mort 2014; Miyata and Kitagawa 2016). Therefore, we next analyzed total and cleaved aggrecan levels in the mouse auditory cortex of adult WT, *Fmr1* KO, $Fmr1^{Flox/y}$, and $Cre^{Nex1}/Fmr1^{Flox/y}$ cKO mice (Fig. 4C). We found that total levels of full-length aggrecan were significantly reduced in both the *Fmr1* KO ($n = 4$, $t(6) = 5.44$, $P = 0.0016$, *t*-test) and $Cre^{Nex1}/Fmr1^{Flox/y}$ cKO mice ($n = 4$, $t(6) = 3.32$, $P = 0.0159$, *t*-test) compared with WT and $Fmr1^{Flox/y}$ mice, respectively (Table 3 and Fig. 4D). In contrast, cleaved aggrecan levels were significantly increased in both the *Fmr1* KO ($n = 4$, $t(6) = 6.40$, $P = 0.0031$, *t*-test) and $Cre^{Nex1}/Fmr1^{Flox/y}$ cKO ($n = 4$, $t(6) = 9.09$, $P < 0.0001$, *t*-test) mice compared with their respective WT counterparts (Table 3 and Fig. 4E). As a result, the cleaved aggrecan to total aggrecan ratio was significantly increased in both the *Fmr1* KO ($n = 4$, $t(6) = 7.25$, $P = 0.0003$, *t*-test) and $Cre^{Nex1}/Fmr1^{Flox/y}$ cKO mice ($n = 3$–4, $t(5) = 8.66$, $P = 0.0001$, *t*-test) compared with WT and $Fmr1^{Flox/y}$ mice, respectively (Table 3 and Fig. 4F). Our data suggest that the loss of FMRP in excitatory neurons contributes to the increased gelatinase activity in adult *Fmr1* KO and $Cre^{Nex1}/Fmr1^{Flox/y}$ cKO mouse auditory cortex that may affect formation of WFA+ PNNs around PV interneurons by cleaving aggrecan.

Deletion of FMRP from Excitatory Neurons Triggers a Decrease in PV Levels, While Akt and mTOR Phosphorylation Is Increased in Auditory Cortex of Adult $Cre^{Nex1}/Fmr1^{Flox/y}$ cKO Mice

Consistent with the reduced PV cell density in adult *Fmr1* KO and $Cre^{Nex1}/Fmr1^{Flox/y}$ cKO mice compared with their controls, we observed a significant decrease in PV levels in the cell lysates from auditory cortex of both *Fmr1* KO ($n = 4$, $t(6) = 32.5$, $P < 0.0001$, *t*-test) and $Cre^{Nex1}/Fmr1^{Flox/y}$ cKO mice ($n = 4$, $t(6) = 4.72$, $P = 0.0032$, *t*-test) compared with their WT counterparts (Table 3 and Fig. 5A,D). This is consistent with previous findings that show a reduction in PV expression in cortex of mouse models of autism (Filice et al. 2016).

Enhanced Akt/mTOR signaling may also underlie changes in synaptic functions and hyperexcitability associated with

Table 3 Summary table showing gelatinase activity and protein levels in the auditory cortex of adult WT, *Fmr1* KO, $Fmr1^{Flox/y}$, and $Cre^{Nex1}/Fmr1^{Flox/y}$ cKO mice (mean ± SEM)

	WT	*Fmr1* KO	$Fmr1^{Flox/y}$	$Cre^{Nex1}/Fmr1^{Flox/y}$ cKO
Gelatinase activity	140.90 ± 28.49	337.40 ± 36.24** ($P = 0.0053$)	77.24 ± 6.71	263.10 ± 46.13** ($P = 0.0072$)
Full-length aggrecan levels	0.73 ± 0.01	0.44 ± 0.05** ($P = 0.0016$)	0.99 ± 0.07	0.67 ± 0.07* ($P = 0.0159$)
Cleaved aggrecan levels	0.96 ± 0.02	1.35 ± 0.04** ($P = 0.0031$)	1.01 ± 0.07	2.14 ± 0.08**** ($P < 0.0001$)
Cleaved/total aggrecan ratio	0.57 ± 0.01	2.21 ± 0.23*** ($P = 0.0003$)	0.99 ± 0.10	3.52 ± 0.27*** ($P = 0.0001$)
PV levels	0.78 ± 0.01	0.32 ± 0.01**** ($P < 0.0001$)	1.02 ± 0.05	0.69 ± 0.05** ($P = 0.0032$)
p-mTOR/mTOR ratio	0.93 ± 0.04	1.28 ± 0.03*** ($P = 0.0005$)	0.96 ± 0.03	1.27 ± 0.07** ($P = 0.0073$)
p-Akt/Akt ratio	1.36 ± 0.04	1.91 ± 0.12** ($P = 0.0051$)	0.97 ± 0.05	1.40 ± 0.02*** ($P = 0.0002$)

Statistical analysis of differences between *Fmr1* KO and $Cre^{Nex1}/Fmr1^{Flox/y}$ cKO mice with their respective WT counterparts was performed using *t*-test (unpaired, two-tailed).
*$P < 0.05$, **$P < 0.01$, ***$P < 0.001$, ****$P < 0.0001$.

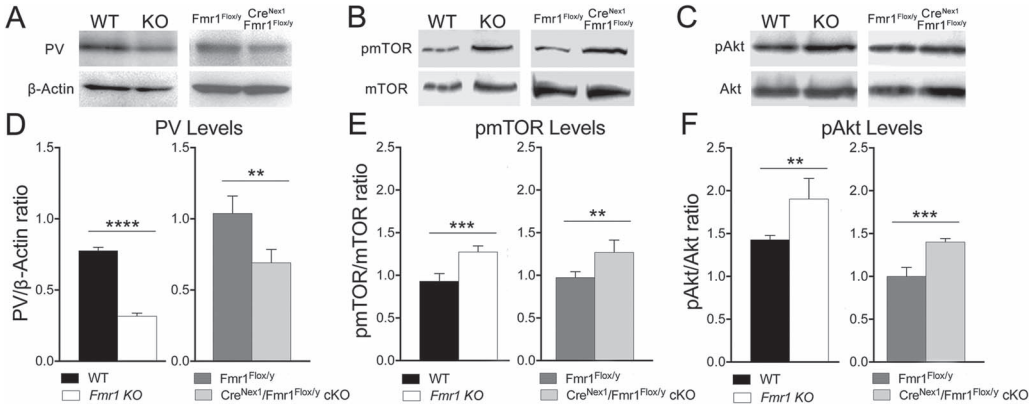

Figure 5. FMRP deletion from forebrain excitatory neurons is sufficient to decrease PV levels and to trigger enhanced Akt and mTOR phosphorylation in the auditory cortex of adult mice. (*A–C*) Western blot showing PV (*A*), p-mTOR and mTOR (*B*), and p-Akt and Akt (*C*) levels in lysates from adult auditory cortex of WT, *Fmr1* KO, $Fmr1^{Flox/y}$, and $Cre^{Nex1}/Fmr1^{Flox/y}$ cKO mice. (*D*) Quantitative analysis of PV levels. Graphs show mean ± SEM ($n = 4$/group, **$P < 0.01$; ****$P < 0.0001$, *t*-test). PV levels are significantly reduced in adult auditory cortex of both *Fmr1* KO and $Cre^{Nex1}/Fmr1^{Flox/y}$ cKO mice compared with their WT counterparts. (*E,F*) Quantitative analysis of p-mTOR/mTOR (*E*) and p-Akt/Akt ratios. Graphs show mean ± SEM ($n = 4$/group, **$P < 0.01$; ***$P < 0.001$, *t*-test). There is a significant increase in the p-mTOR/mTOR ratio in the *Fmr1* KO mice compared with WT (*E*). There is also a significant increase in the p-Akt/Akt ratio in the *Fmr1* KO mice compared with WT mice (*F*). Similarly, there is a significant increase in the p-mTOR/mTOR ratio (*E*) and p-Akt/Akt ratio (*F*) in the adult auditory cortex of $Cre^{Nex1}/Fmr1^{Flox/y}$ cKO mice compared with $Fmr1^{Flox/y}$ mice.

FXS and other autistic spectrum disorders (Klann and Dever 2004; Sharma et al. 2010; Enriquez-Barreto and Morales 2016; Sato 2016). Therefore, we investigated Akt/mTOR activation in adult auditory cortex of global *Fmr1* KO and forebrain excitatory neuron-specific $Cre^{Nex1}/Fmr1^{Flox/y}$ cKO mice, by examining mTOR and Akt phosphorylation levels (Table 3 and Fig. 5B,C). Higher levels of the phosphorylated (i.e., active) forms of both proteins were detected in the adult auditory cortex of *Fmr1* KO mice compared with WT. Specifically, there was a 33% increase in the p-mTOR/mTOR ratio in the *Fmr1* KO mice ($n = 4$, $t(6) = 6.89$, $P = 0.0005$, *t*-test) compared with WT (Table 3 and Fig. 5E). A similar effect was also seen for the p-Akt/Akt ratio, which was 35% higher in the *Fmr1* KO mice ($n = 4$, $t(6) = 4.30$, $P = 0.0051$, *t*-test) compared with WT mice (Table 3; Fig. 5F). Similar changes were seen in the auditory cortex of adult $Cre^{Nex1}/Fmr1^{Flox/y}$ cKO mice compared with control $Fmr1^{Flox/y}$ mice. There was a 30% increase in the p-mTOR/mTOR ratio ($n = 4$, $t(6) = 3.97$, $P = 0.0073$, *t*-test) (Table 3 and Fig. 5E) and a 40% increase in the p-Akt/Akt ratio in the $Cre^{Nex1}/Fmr1^{Flox/y}$ cKO mice ($n = 4$, $t(6) = 7.86$, $P = 0.0002$, *t*-test) (Table 3 and Fig. 5F) compared with $Fmr1^{Flox/y}$ mice. These results demonstrate that FMRP deletion from forebrain excitatory neurons is sufficient to trigger enhanced Akt and mTOR phosphorylation in the auditory cortex of adult mice.

Resting EEG Gamma Power Is Enhanced in the Auditory Cortex of Adult $Cre^{Nex1}/Fmr1^{Flox/y}$ cKO Mice

If impaired formation of WFA+ PNNs around PV interneurons and enhanced gelatinase activity in the auditory cortex underlie abnormal neural oscillations observed in the global *Fmr1* KO mice (Wen et al. 2018a; Lovelace et al. 2018), then we should see similar deficits in forebrain excitatory neuron–specific $Cre^{Nex1}/Fmr1^{Flox/y}$ cKO mice. However, it is also possible that some of these electrophysiological deficits are inherited from loss of FMRP from other cell types or subcortical sites (Strumbos et al. 2010; Beebe et al. 2014; Wang et al. 2014; Rotschafer et al. 2015; Garcia-Pino et al. 2017). Therefore, we quantified EEG responses in $Cre^{Nex1}/Fmr1^{Flox/y}$ cKO mice.

Baseline EEG raw power was calculated in auditory cortex of control $Fmr1^{Flox/y}$ ($n = 9$) and $Cre^{Nex1}/Fmr1^{Flox/y}$ cKO ($n = 9$) mice by analyzing all frequency bands during the entire 5-min resting period. Examples of 1-s segments of resting EEG for each genotype, as well as genotype averages (±SEM) of power spectra, are depicted in Figure 6. Even in the raw traces (Fig. 6A), enhanced high frequency oscillations are apparent in auditory cortex. The group average power spectral densities are shown in Figure 6B, wherein genotype differences in auditory cortex can

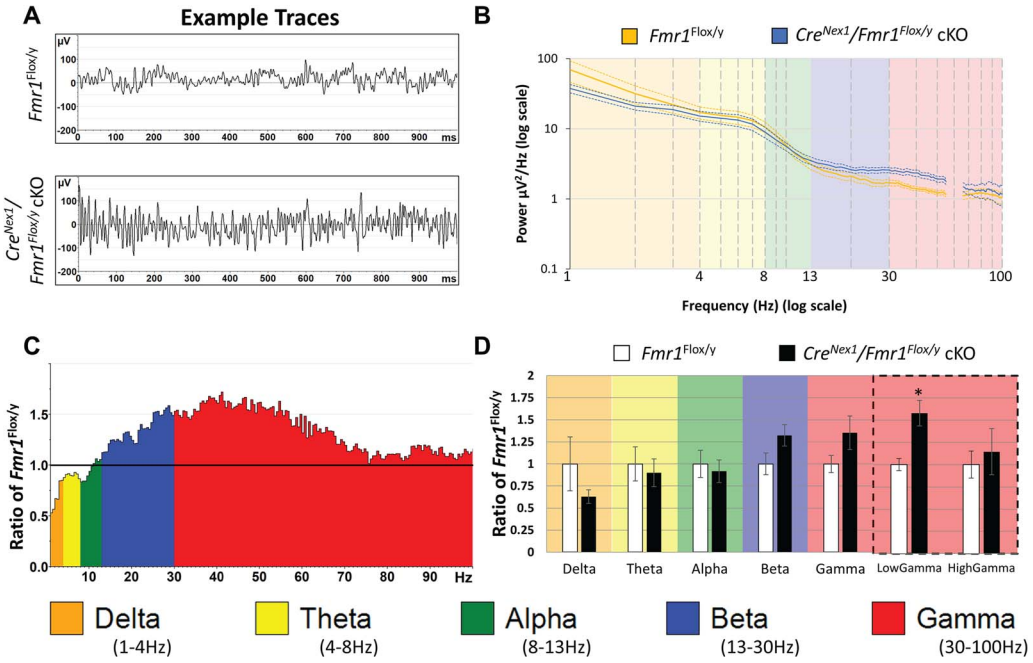

Figure 6. Forebrain excitatory neuron-specific deletion of *Fmr1* reveals increased low-gamma power in auditory cortex of adult mice. Five minutes of baseline EEG data (in the absence of auditory stimulation) from electrodes implanted in the auditory cortex of $Fmr1^{Flox/y}$ ($n = 9$) and $Cre^{Nex1}/Fmr1^{Flox/y}$ cKO mice ($n = 9$) was recorded and FFT analysis was done to determine spectral power. (*A*) Depicted are examples of such segments from control $Fmr1^{Flox/y}$ (A, top) and $Cre^{Nex1}/Fmr1^{Flox/y}$ cKO (A, bottom) mice auditory cortex. (*B*) Power density (μV^2/Hz) was calculated for each artifact-free segment using FFT, followed by averaging of all segments for a given mouse. These individual averages then contributed to the genotype grand average for each genotype ($n = 9$ per genotype). Significant differences between genotypes are observed in auditory cortex at low-gamma frequencies (30–55 Hz). Note: Frequencies from 55 to 65 Hz were excluded in "all" analysis, as a 60-Hz notch filter was utilized to eliminate line noise. (*C*) Average power in the $Cre^{Nex1}/Fmr1^{Flox/y}$ cKO mouse auditory cortex is expressed as the ratio of control levels ($Fmr1^{Flox/y}$). A value of 1 (horizontal black line) indicates no mean difference in power at that frequency between genotypes, while values above the black line indicate $Cre^{Nex1}/Fmr1^{Flox/y}$ cKO > $Fmr1^{Flox/y}$ and below the black line indicates $Cre^{Nex1}/Fmr1^{Flox/y}$ cKO < $Fmr1^{Flox/y}$. (*D*) Auditory cortex values were divided into standard frequency bands. MANCOVA analysis controlling for the effect of movement, revealed differences in the low gamma range of auditory cortex after Bonferroni correction for multiple comparisons. $^*P < 0.05$.

be seen at frequencies ~40 Hz (Fig. 6B). Statistical analysis was performed using a one-way MANCOVA approach with percentage time spent moving as a covariate. We compared genotype mean differences on 6 bands per region: delta (1–4 Hz), theta (4–10 Hz), alpha (10–13 Hz), beta (13–30 Hz), low gamma (30–55 Hz), and high gamma (65–100 Hz). The gamma band (30–100 Hz) was divided because multiple studies suggest that low (30–60 Hz) versus high frequency (>60 Hz) bands in gamma range may arise from different mechanisms (Ray and Maunsell 2011; Balakrishnan and Pearce 2014; Dvorak and Fenton 2014). Using this approach, we confirmed assumptions of equality of covariance using Box's M, $P = 0.089$, as well as Levene's test of equality of error variance, no differences between genotypes were observed in error variance (all $P > 0.05$). Since assumptions were not violated, we report an effect of genotype (Pillai's trace = 0.738, $P = 0.016$) across all 6 of the combined frequency variables, which include movement as a covariate. We then determined that the only individual frequency band difference between genotypes in the auditory cortex of $Cre^{Nex1}/Fmr1^{Flox/y}$ cKO mice was in the low gamma band (Fig. 6C,D). Low gamma was significantly increased after correction for multiple comparisons: auditory cortex low gamma, $F(1,15) = 12.258$, $P = 0.0032$, $\eta^2 = 0.45$. These data lead to the interpretation that the auditory cortex low gamma differences in the global *Fmr1* KO mice likely arise due to local circuit defects. Gamma power is influenced, at least in part, by PV+ interneuron function in the cortex (Sohal et al. 2009). Observed increased gelatinase activity along with reduced PV+ cell density and WFA+ PNNs around PV+ neurons is likely involved in the local circuit dysfunction and increased low-gamma power reported here.

Gamma Synchronization Is Not Affected in Adult $Cre^{Nex1}/Fmr1^{Flox/y}$ cKO Mouse Auditory Cortex

We hypothesized that the increased baseline gamma in $Cre^{Nex1}/Fmr1^{Flox/y}$ cKO mouse auditory cortex would lead to a deficit in generating consistent phase locking in gamma frequencies across trials. This is because the observed increased gamma power during rest (no auditory stimulation) may act as "noise" and interfere with consistency of sound-evoked responses from trial to trial. Both up and down chirps were tested to ensure that the differences are specific to modulation frequencies and are not affected by the direction of frequency change in the sound. Briefly, a "chirp" stimulus is a broadband noise, which is amplitude modulated over the course of its duration (2 s). The rate of modulation either goes from 100 Hz down to 1 Hz over 2 s (down-chirp) or goes from 1 Hz up to 100 Hz over 2 s (up-chirp, see Fig. 7, bottom). After repeated chirp presentation (300 trials for up, 300 for down), the ITPC was calculated across trials in the time X frequency domain using Morlet Wavelet analysis, similar to our previously published results (Lovelace et al. 2018). After grand average ITPC was calculated for each group, means for $Fmr1^{Flox/y}$ mice ($n = 9$) were subtracted from the means for $Cre^{Nex1}/Fmr1^{Flox/y}$ cKO ($n = 9$; Fig. 7A, only "up"-chirp data are shown). For statistical comparisons, nonparametric cluster analysis was used to

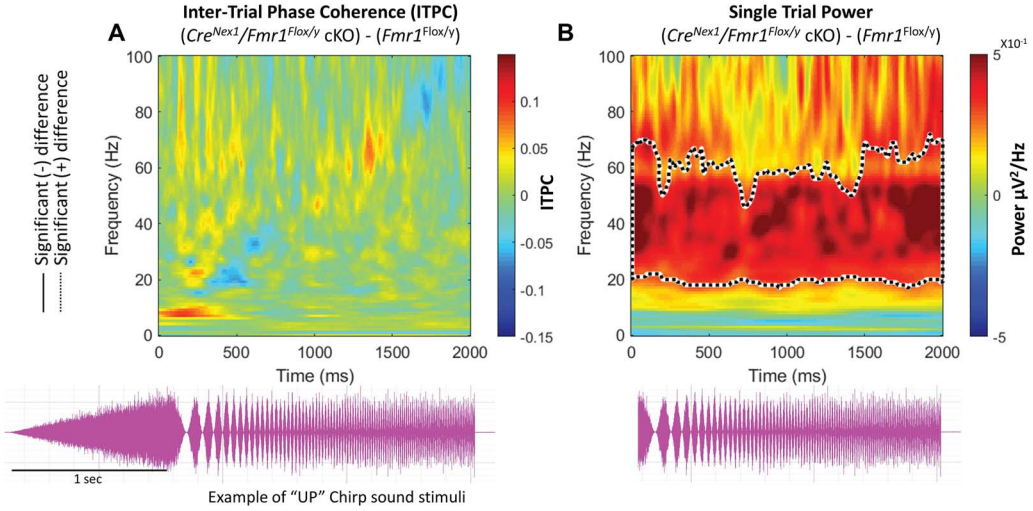

Figure 7. Adult $Cre^{Nex1}/Fmr1^{Flox/y}$ cKO mice show no phenotype in phase locking to auditory "up-chirp" stimuli, but non–phase-locked STP was enhanced. (*A*) Trains of chirp modulated broadband noise (bottom) were presented to each mouse 300 times. For each mouse, ITPC was measured to determine the degree of phase locking across trials. Grand average matrices were calculated for each genotype and then $Fmr1^{Flox/y}$ ($n = 9$) ITPC values were subtracted from $Cre^{Nex1}/Fmr1^{Flox/y}$ cKO ($n = 9$) values. Blue areas indicating $Cre^{Nex1}/Fmr1^{Flox/y}$ cKO < $Fmr1^{Flox/y}$, green areas no difference, and red $Cre^{Nex1}/Fmr1^{Flox/y}$ cKO > $Fmr1^{Flox/y}$. Statistical cluster analysis reveals contiguous time × frequency regions that are significantly different between genotypes. Black solid contours (mean negative group difference) and black dashed contours (mean positive group difference) indicate these significant clusters. After subtraction and cluster analysis in auditory cortex, $Cre^{Nex1}/Fmr1^{Flox/y}$ cKO mice express no statistically significant changes in ITPC along the diagonal band elicited by the up-chirp. (*B*) For each mouse, STP was measured to determine the average total non–phase-locked power during sound presentation. Grand average matrices were calculated for each genotype and then $Fmr1^{Flox/y}$ ($n = 9$) STP values were subtracted from $Cre^{Nex1}/Fmr1^{Flox/y}$ cKO ($n = 9$) values. Blue areas indicating $Cre^{Nex1}/Fmr1^{Flox/y}$ cKO < $Fmr1^{Flox/y}$, green areas no difference, and red $Cre^{Nex1}/Fmr1^{Flox/y}$ cKO > $Fmr1^{Flox/y}$. Statistical cluster analysis reveals contiguous time × frequency regions that are significantly different between genotypes. Black dashed contour indicate these significant clusters. After subtraction and cluster analysis in auditory cortex, $Cre^{Nex1}/Fmr1^{Flox/y}$ cKO mice express statistically significant increase in STP throughout the sound presentation in the low gamma range (~20–60 Hz), consistent with resting EEG analysis.

determine contiguous regions in the time X frequency domain that were statistically different between genotypes (Fig. 7A). We observed no significant differences in gamma band ITPC in the auditory cortex of $Cre^{Nex1}/Fmr1^{Flox/y}$ cKO mice (Fig. 7A). Similar patterns and statistics of ITPC were observed for both up- and down-chirps (down-chirp data not shown). These data show that the gamma synchronization deficits observed in the global *Fmr1* KO mouse auditory cortex are not due to abnormal expression of FMRP in forebrain excitatory neurons. Either other cell types in the cortex are specifically involved in the consistency of phasic responses to amplitude-modulated noise (e.g., FMRP expressed in astrocytes or GABAergic neurons) or the ITPC deficit found in the global *Fmr1* KO is inherited from subcortical sites wherein neurons phase lock to faster amplitude modulation rates than the cortex.

Increased Non–Phase-Locked STP Is Observed in the Auditory Cortex of Adult $Cre^{Nex1}/Fmr1^{Flox/y}$ cKO Mice during Chirp Stimulation

We investigated non–phase-locked STP during the chirp stimulation period (Fig. 7B), because we previously reported a significant increase in STP in the global *Fmr1* KO mouse. An increase in STP is also seen in humans with FXS (Ethridge et al. 2017). Using the same statistical cluster analysis as for the chirp ITPC, the $Cre^{Nex1}/Fmr1^{Flox/y}$ cKO mice showed an increase in background gamma power in the auditory cortex and only in the lower gamma band (Fig. 7B). These data suggest that low-gamma deficits in non–phase-locked power in the auditory cortex are due to deficits in local circuits mediated by abnormal FMRP in cortical excitatory neurons. This also suggests that the low-gamma power increase during silence (Fig. 6, resting EEG data) is still present throughout sound presentation.

Induced Power Is Significantly Enhanced in the Auditory Cortex of Adult $Cre^{Nex1}/Fmr1^{Flox/y}$ cKO Mice

In addition to phase locking to the auditory chirp, we also compared genotypes on auditory cortex responses with 100 trains of brief broadband noise stimulus (100 ms each noise burst, 10 stimuli per train). We tested both a habituating rate of presentation (4 Hz) and a nonhabituating rate (0.25 Hz) (Lovelace et al. 2016). Example traces of single sound presentation for both genotypes are shown in Figure 8A and the first 4 stimuli in the 4-Hz train in Fig. 8D. We measured both ITPC and induced power (baseline corrected non–phase-locked single trial power) for each repetition rate. First, the ITPC for the nonhabituation 0.25 Hz rate showed a reduction in phase locking in the beta range (~20–30 Hz) immediately after sound presentation (Fig. 8B). This suggests that $Cre^{Nex1}/Fmr1^{Flox/y}$ cKO mice are more variable in their ERP latencies compared with control $Fmr1^{Flox/y}$ mice at those specific frequencies. In addition, $Cre^{Nex1}/Fmr1^{Flox/y}$ cKO mice displayed an increase in induced power ~100 ms following the onset of the sound from the beta to low gamma range (~10–50 Hz) (Fig. 8C). This result is indicative of increased "ongoing" response after the initial onset ERP (Rotschafer and Razak 2013). Using the same analysis on the first 4 responses to a 4-Hz train of sounds reveals the same ITPC deficit for the first sound in the train (reduction in ITPC from ~20 to 30 Hz), with no difference during the rest of the train (Fig. 8E). However, after repeated sound stimulation, the ongoing non–phase-locked power persists throughout the entire train presentation (Fig. 8F). This effect is visually apparent in the example traces

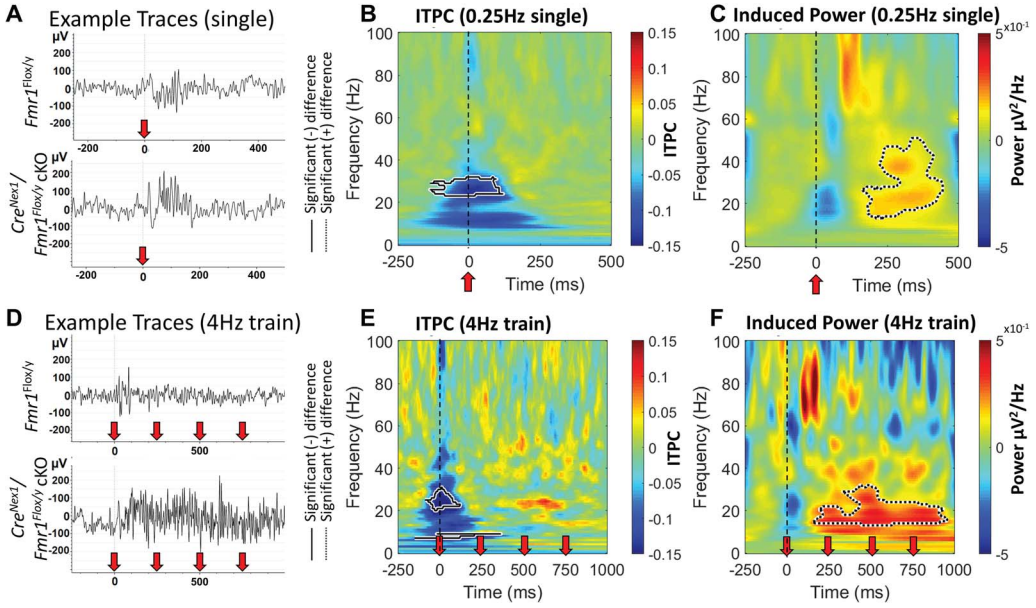

Figure 8. Increase in induced (non–phase-locked) power is seen in adult $Cre^{Nex1}/Fmr1^{Flox/y}$ cKO mice. (*A*) Example traces in response to single sound presentations at 0.25 Hz from both genotypes. Red arrow indicates onset of 100 ms broadband noise. (B) Grand average difference plot of ITPC during single-sound presentations between genotypes ($Cre^{Nex1}/Fmr1^{Flox/y}$ cKO—$Fmr1^{Flox/y}$). There is a reduction (solid line contour) in ITPC in the $Cre^{Nex1}/Fmr1^{Flox/y}$ cKO mice ~20–30 Hz immediately after sound presentation. (*C*) Baseline corrected STP (induced power) was calculated for each genotype and difference plot is shown. Increased induced power (dashed line contours) is observed following the initial ERP response, indicating increased "ongoing" activity after sound presentation. (*D*) Example traces of 4 Hz sound presentation for both genotypes. Only the first four noise bursts of each train were analyzed. (*E*) ITPC differences were observed for the first sound in the train in the same range as seen in the single response in B, but no differences were seen with subsequent sound presentation at 4 Hz. (*F*) Increased induced power was observed after the first sound presentation and persisted with subsequent sounds. This effect is also apparent in the example traces in D.

shown in Fig. 8D, where the $Cre^{Nex1}/Fmr1^{Flox/y}$ cKO mouse shows persistent high-frequency oscillations throughout the sound train, while the control $Fmr1^{Flox/y}$ mouse is relatively quiet. These combined results indicate that the variability of latencies to the onset of sound is increased (reduction in ITPC) when FMRP is removed from excitatory cortical neurons, and suppression of ongoing activity is reduced in the auditory cortex both after single sound presentation and repeated presentations.

Excitatory Neuron-Specific Adult $Cre^{Nex1}/Fmr1^{Flox/y}$ cKO Mice Display Increased Locomotor Activity, but No Anxiety-Like Behavior

Adult male $Fmr1^{Flox/y}$ ($n = 6$) and $Cre^{Nex1}/Fmr1^{Flox/y}$ cKO ($n = 6$) mice were tested for locomotor activity and anxiety in an elevated plus maze by measuring total number of entries or speed and time spent in open arms, respectively (Table 4 and Fig. 9). $Cre^{Nex1}/Fmr1^{Flox/y}$ cKO mice demonstrated increased locomotor activity by making significantly more total arm entries than $Fmr1^{Flox/y}$ mice ($n = 6$, $t(10) = 2.61$, $P = 0.0262$, *t*-test) (Table 4 and Fig. 9A) and by showing a significant increase in speed ($n = 6$, $t(10) = 3.44$, $P = 0.0063$, *t*-test) (Table 4 and Fig. 9B). However, $Cre^{Nex1}/Fmr1^{Flox/y}$ cKO mice showed no difference in time spent in open arm per entry ($n = 6$, $P = 0.273$, *t*-test) or percentage of time in open arms ($n = 6$, $P = 0.0521$, *t*-test) compared with $Fmr1^{Flox/y}$ mice (Table 4 and Fig. 9C,D).

We used an OF test as another gauge of locomotor activity and anxiety, by determining total number of lines crosses or speed and the tendency of mice to travel through the center of an open field or the time in thigmotaxis, respectively. Similar to the performance in the elevated plus maze, $Cre^{Nex1}/Fmr1^{Flox/y}$ cKO mice showed increased locomotor activity with significantly more line crosses ($n = 6$, $t(10) = 4.36$, $P = 0.0014$, *t*-test) (Table 4 and Fig. 9E) and increased speed ($n = 6$, $t(10) = 3.65$, $P = 0.0045$, *t*-test) (Table 4 and Fig. 9F) than $Fmr1^{Flox/y}$ mice. However, there was no significant difference in time spent in the center per entry ($n = 6$, $P = 0.862$, *t*-test) or percentage of time in thigmotaxis ($n = 6$, $P = 0.183$, *t*-test) between the two groups (Table 4 and Fig. 9G,H). These findings establish that FMRP deletion from forebrain excitatory neurons increases locomotor activity but has no effect on anxiety-like behaviors.

Table 4 Summary table showing locomotor activity and *anxiety* measures of $Fmr1^{Flox/y}$ and $Cre^{Nex1}/Fmr1^{Flox/y}$ cKO mice using elevated plus (EP) maze and OF behavior tests (mean ± SEM)

	$Fmr1^{Flox/y}$	$Cre^{Nex1}/Fmr1^{Flox/y}$ cKO
Total entries (EP)	13 ± 2	23 ± 3* ($P = 0.0262$)
Speed (EP)	21.99 ± 2.37	31.18 ± 1.23** ($P = 0.0063$)
Time spent in open arm/entry (EP)	5.65 ± 0.49	6.41 ± 0.43
% Time in open arms (EP)	14.15 ± 0.99	18.92 ± 1.92
Total line crosses (OF)	238 ± 9	321 ± 17** ($P = 0.0014$)
Speed (OF)	50.72 ± 2.46	67.90 ± 4.02** ($P = 0.0045$)
Time spent in center/entry (OF)	0.72 ± 0.12	0.69 ± 0.10
% Time in thigmotaxis (OF)	54.30 ± 1.66	50.58 ± 1.99

Statistical analysis of differences between $Cre^{Nex1}/Fmr1^{Flox/y}$ cKO mice and their WT counterparts was performed using *t*-test (unpaired, two-tailed).
*$P < 0.05$, **$P < 0.01$.

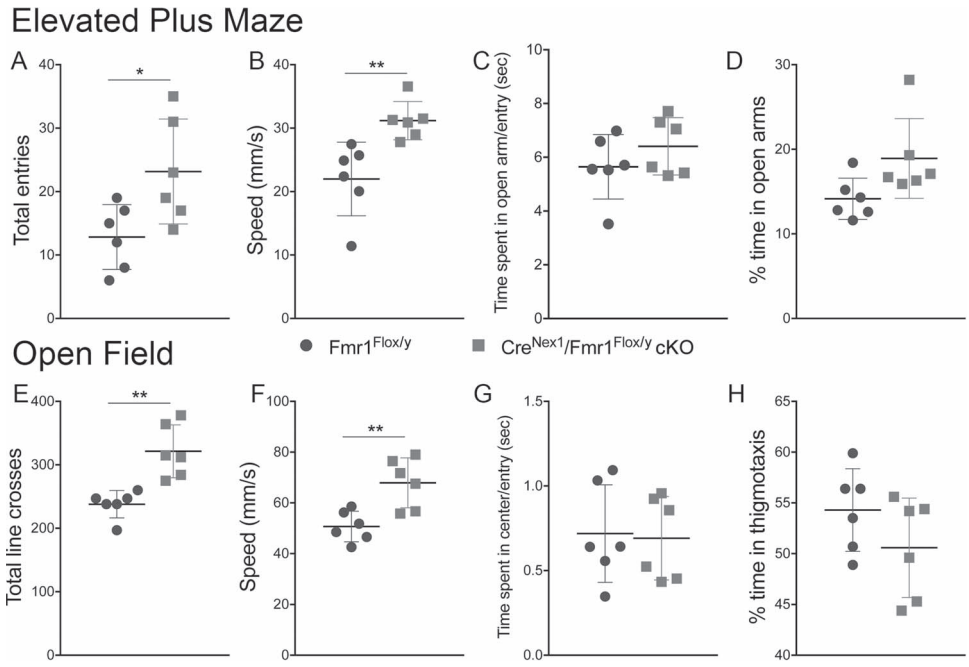

Figure 9. Adult excitatory neuron–specific $Cre^{Nex1}/Fmr1^{Flox/y}$ cKO mice display increased locomotor activity, but no anxiety-like behavior. (*A–D*) Graphs demonstrate the performance of $Cre^{Nex1}/Fmr1^{Flox/y}$ cKO mice in the elevated plus maze as measured by the total number of arm entries (*A*), speed (*B*), the total amount of time spent in the open arm per entry (*C*), and the percent of time spent in the open arms (*D*). Graphs show mean ± SEM ($n = 6$/group, $^{*}P < 0.05$; $^{**}P < 0.01$, *t*-test). (*E–H*) Graphs demonstrate the performance of $Cre^{Nex1}/Fmr1^{Flox/y}$ cKO mice in the open field as measured by the total number of line crosses (*E*), speed (*F*), the amount of time spent in the center per entry (*G*), and the percent time spent in thigmotaxis (*H*). Graphs show mean ± SEM ($n = 6$/group, $^{**}P < 0.01$, *t*-test).

Discussion

Sensory processing deficits commonly co-occur with ASD. The mechanisms of sensory deficits in autism remain poorly understood, and no current therapies are available to alleviate sensory symptoms. The main findings of this study provide novel insights into mechanisms of sensory processing issues in FXS, a leading genetic cause of autism (summarized in Fig. 10). We show that cell type-specific deletion of *Fmr1* from forebrain excitatory neurons is sufficient to trigger an abnormal EEG phenotype in the adult auditory cortex, such as increased power of resting low-gamma oscillations. In addition, we show that deletion of *Fmr1* from forebrain excitatory neurons elicits elevated gelatinase activity, higher mTOR/Akt phosphorylation, and impaired PV/PNN colocalization in the auditory cortex. While both astrocytes and neurons can release gelatinases MMP-2 and MMP-9 (Yong et al. 1998; Szklarczyk et al. 2002; Murase et al. 2016), our data suggest that loss of FMRP from excitatory neurons is sufficient to trigger increased gelatinase activity, which may affect the formation of WFA+ PNNs around PV interneurons.

Abnormal density and function of PV+ GABAergic interneurons appear to be a common finding across sensory cortices in FXS model mice and may be a common mechanism for abnormal sensory processing and sensitivity (Selby et al. 2007; Contractor et al. 2015; Goel et al. 2018; Wen et al. 2018a, b). PV expression in inhibitory neurons is activity-dependent (Patz et al. 2004; Chang et al. 2010). The reduction in PV expression in $Cre^{Nex1}/Fmr1^{Flox/y}$ cKO mouse auditory cortex may occur due to reduced excitatory drive onto these neurons. In vitro slice physiology studies of somatosensory cortex in global *Fmr1* KO mice have shown local circuit deficits with reduced excitatory input received by PV interneurons, whereas excitatory

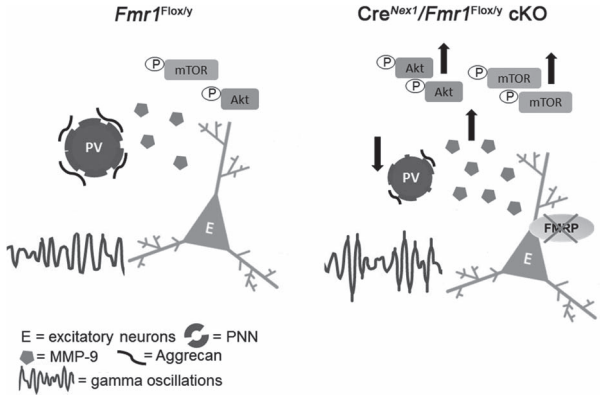

Figure 10. Schematic of cellular and EEG phenotypes in the auditory cortex of adult $Cre^{Nex1}/Fmr1^{Flox/y}$ cKO compared with $Fmr1^{Flox/y}$ mice. Left panel depicts normal cellular and EEG phenotypes in the auditory cortex of $Fmr1^{Flox/y}$ mice. Right panel depicts reduced PV levels, impaired formation of WFA+ PNNs around PV cells, increased gelatinase activity and mTOR/Akt phosphorylation, and abnormal neural oscillations in auditory cortex of excitatory neuron–specific $Cre^{Nex1}/Fmr1^{Flox/y}$ cKO mice.

and inhibitory drive onto excitatory neurons was normal (Gibson et al. 2008). Consistent with our data, these deficits are seen following removal of FMRP just from excitatory neurons, suggesting that a common mechanism across sensory cortices in *Fmr1* KO mice is reduced excitation of PV cells (Selby et al. 2007; Contractor et al. 2015; Goel et al. 2018). A second reason for altered PV cell function might be through the degradation of aggrecan-containing WFA+ PNNs. In the cerebral cortex, PNN loss around PV cells reduces excitability of these cells

(Balmer 2016; Lensjø et al. 2017; Wen et al. 2018a). Therefore, degradation of PNN is predicted to decrease excitability of PV cells leading to hyperexcitability of cortical networks and abnormal neural oscillations. PNNs protect PV cells from oxidative stress, and the loss of PNNs may lead to PV cell death (Cabungcal et al. 2013).

The decrease in PV cell number and function is predicted to have major implications for processing of auditory input in the cortex and may, at least partially, underlie auditory hypersensitivity. PV+ neurons comprise nearly 50% of all GABAergic cells in the neocortex, and individual PV+ neurons can provide synchronized inhibition on to multiple pyramidal cells contributing to network activity levels and patterns (Packer and Yuste 2011). PV+ neurons are involved in gain control in the auditory cortex and shape how neurons respond to increasing sound levels (Moore and Wehr 2013), suggesting a possible neural correlate of abnormal auditory sensitivity. Reduction of PV expression causes GABA neuron dysfunction and facilitation in response to repetitive stimulation, particularly at gamma frequencies (Lucas et al. 2010). Rapid spiking, putative, PV+ cells are also linked to processing of rapid spectrotemporal changes in acoustic inputs (Atencio and Schreiner 2008) and may be linked to the reduced selectivity for frequency-modulated sweep rates in *Fmr1* KO mouse auditory cortex (Rotschafer and Razak 2013). Cortical gamma oscillations are linked to the function of PV+ interneurons (Gonzalez-Burgos and Lewis 2008; Cardin et al. 2009; Sohal et al. 2009; Volman et al. 2011; Carlén et al. 2012; Keeley et al. 2017). Gamma band activity is involved in a broad array of sensory and cognitive processes, several of which are affected in FXS. The gamma phase–locking deficits may cause sensory discrimination deficits (Cardin et al. 2009; Sohal et al. 2009) that may lead to delayed language and cognitive development in FXS. Low-frequency oscillations are involved in attention processes and can modulate high-frequency oscillations, which can be abnormal in *Fmr1* KO mice (Radwan et al. 2016).

Our finding of correlated reduction in PV/PNN density and increase in low-gamma power may, at least at the superficial level, seem inconsistent with studies that suggest PV cell activity increases gamma oscillations (Sohal et al. 2009). However, a number of recent studies have suggested that the relationship between interneuron activity and oscillations is complex, and include disinhibitory and compensatory mechanisms (Tsodyks et al. 1997; Ozeki et al. 2009). For example, decreased excitatory drive onto PV interneurons in a Schizophrenia model resulted in increased gamma oscillations and, interestingly, increased locomotor activity (Del Pino et al. 2013). Acute rhythmic stimulation of PV cells using optogenetics in vivo can generate neural oscillations at gamma frequencies, but not at other frequencies (Cardin et al. 2009). However, somatostatin (SOM) interneurons are also shown to be critical for stimulus-induced gamma rhythms in the visual cortex (Veit et al. 2017). While both PV and SOM interneurons contribute to gamma oscillations, it is possible that prolonged loss of PV cells may trigger an increase in SOM interneuron firing and synchronized gamma oscillations to compensate for the change in E-I balance reflecting homeostatic stabilization of the circuits (Antoine et al. 2019).

Within the broadband gamma oscillations (30–100 Hz), only the low gamma band power is increased in the auditory cortex of $Cre^{Nex1}/Fmr1^{Flox/y}$ cKO mice. The differential effects on gamma frequencies are consistent with multiple studies suggesting different mechanisms responsible for generating low gamma (~30–60 Hz) and high gamma (60–120 Hz) (Ray and Maunsell 2011; Balakrishnan and Pearce 2014; Dvorak and Fenton 2014). Ray and Maunsell (2011) suggested that the low gamma band reflects true oscillations that arise through PV neuron firing and synchronization of pyramidal cell activity, whereas the higher gamma frequencies reflect irregular spiking activity near the electrodes.

FMRP is expressed in multiple regions of the auditory pathway (Zorio et al. 2017). Abnormal auditory processing and plasticity have been reported in the brainstem (Chen and Toth 2001; Strumbos et al. 2010; Wang et al. 2014; Rotschafer et al. 2015) and auditory cortex (Kim et al. 2013; Rotschafer and Razak 2013; Lovelace et al. 2016; Sinclair et al. 2017; Lovelace et al. 2018) of global *Fmr1* KO mice. The abnormal responses seen in the cortex may be inherited from deficits in subcortical sites and/or created de novo due to local cortical circuit deficits. Our data show that *Fmr1* deletion in forebrain excitatory neuron is sufficient to elicit enhanced resting low-frequency gamma power in the auditory cortex. However, resting EEG high-gamma power and chirp-elicited phase locking factor were relatively normal in the $Cre^{Nex1}/Fmr1^{Flox/y}$ cKO mice. Together, these data suggest that both cortical and sub-cortical structures contribute to changes in physiological responses observed in the auditory cortex of *Fmr1* KO mice. Because the auditory system consists of a number of feed-forward and feedback loops, potential for nonlinear interactions in terms of cortical deficits influencing sub-cortical processing cannot be discounted. To begin gaining a systems-level understanding of sensory deficits in autism, future studies will address the effects of *Fmr1* deletion in other cortical cell types and brain areas. Global *Fmr1* KO mice in which *Fmr1* is specifically re-expressed only in the forebrain excitatory neurons and mouse models in which *Fmr1* is specifically deleted in inhibitory neurons, astrocytes, or auditory brainstem would help to shed light on the underlying circuit level mechanisms.

Role of Enhanced Gelatinase Activity in $Cre^{Nex1}/Fmr1^{Flox/y}$ cKO Mice

PNNs are comprised of hyaluronan, glycoproteins, and CSPGs and form a net-like structure on the cell body and proximal dendrites of PV-expressing GABAergic interneurons. Among CSPGs present in PNNs, aggrecan is found almost exclusively in PNNs formed around PV cells (McRae et al. 2007; McRae et al. 2010; Morawski et al. 2012), and excessive proteolytic activity of gelatinases MMP-2 and MMP-9 may affect formation of PNNs and PV functions by cleaving aggrecan (d'Ortho et al. 1997). Indeed in our studies, we observed enhanced gelatinase activity and increased cleavage of aggrecan in the auditory cortex of $Cre^{Nex1}/Fmr1^{Flox/y}$ cKO mice. Consistent with our previous studies in the developing auditory cortex of global *Fmr1* KO mice (Wen et al. 2018a), we found that gelatinase activity was also significantly increased in the adult auditory cortex of both *Fmr1* KO and $Cre^{Nex1}/Fmr1^{Flox/y}$ cKO mice, suggesting that the deletion of FMRP from excitatory neurons is sufficient to increase gelatinase activity in the auditory cortex. Our studies suggest that aggrecan cleavage by MMP-9 is likely responsible for impaired formation of WFA+ PNNs around PV interneurons observed in adult auditory cortex of forebrain excitatory neuron-specific $Cre^{Nex1}/Fmr1^{Flox/y}$ cKO mice.

MMP-9 can also regulate mTOR and Akt activation (Sidhu et al. 2014), potentially through integrins or BDNF/TrkB signaling (Hwang et al. 2005; Yang et al. 2009). Enhanced PI3K-Akt-mTOR signaling is implicated in FXS and may contribute to hyperexcitability by regulating protein synthesis through elongation factor 1α (Hou and Klann 2004; Ronesi and Huber 2008; Sharma et al. 2010; Gross et al. 2011; Hoeffer et al. 2012). The role of

MMP-9 in FXS symptoms is further supported by the fact that the genetic deletion of MMP-9 activity in the brain of *Fmr1* KO mice restored dendritic spine development and mGluR5-dependent LTD in the hippocampus (Sidhu et al. 2014). In addition, MMP-9 reduction in the auditory cortex of *Fmr1* KO mice normalized auditory responses and the formation of WFA+ PNNs around PV cells in the *Fmr1* KO mice to WT levels (Wen et al. 2018a). MMP-9 deletion or reduction in the *Fmr1* KO mice also reversed ERP N1 amplitude habituation deficits (Lovelace et al. 2016) and reduced hyperexcitability in the developing auditory cortex (Wen et al. 2018a), respectively. Minocycline, which is known to inhibit MMP-9 activity beside its antibiotic effects, was shown to reduce FXS symptoms in both humans (Schneider et al. 2013) and mice (Rotschafer et al. 2012; Dansie et al. 2013), further supporting the therapeutically targeting MMP-9 to alleviate FXS symptoms. While the present study suggests that loss of FMRP expression in excitatory neurons is sufficient to enhance gelatinase activity and affect formation of WFA+ PNNs around PV cells, the effects may be indirect and excitatory neurons may also modulate release of MMP-9 or MMP-2 from astrocytes. Future studies will test the role of astrocytes in regulating MMP-9 activity, PNNs, and functional responses in the auditory cortex of the *Fmr1* KO mice.

Increased anxiety and locomotor activity are among the most consistent behavioral symptoms in individuals with FXS (Tranfaglia 2011). However, our studies show that forebrain excitatory neuron-specific $Cre^{Nex1}/Fmr1^{Flox/y}$ cKO mice only exhibit increased locomotor activity, but no anxiety-like behaviors. The auditory brainstem expresses high FMRP levels (Wang et al. 2014), and abnormal sensory processing at the level of the auditory brainstem may underlie the enhanced susceptibility to audiogenic seizures (Chen and Toth 2001). FMRP may regulate neuronal excitability through the direct interactions with several ion channels, such as sodium-activated potassium channel Slack, presynaptic N-type voltage-gated calcium channels, and calcium-activated potassium BK channels (Brown et al. 2010; Zhang et al. 2012; Deng et al. 2013; Ferron et al. 2014; Hébert et al. 2014; Myrick et al. 2015). The enhanced excitability is associated with behavioral symptoms observed in FXS, such as hyperactivity, anxiety, and seizures (Penagarikano et al. 2007; Braat and Kooy 2015). Brainstem noradrenergic and serotoninergic systems may also contribute to anxiety phenotypes in FXS, which may be unaffected in the forebrain-specific deletion model. Taken together, our results suggest the role of subcortical areas in regulating anxiety-like behaviors in global *Fmr1* KO mice as forebrain excitatory neuron-specific deletion of FMRP is not sufficient to trigger this abnormal behavior. On the other hand, abnormal locomotor activity may depend on cortex-specific functions of FMRP.

FMRP loss from excitatory neurons in hippocampus and frontal cortex may also contribute to abnormal behaviors observed in *Fmr1* KO mice, such as hyperactivity, obsessive-compulsive behaviors, and learning and memory deficits (Dansie et al. 2013, Santos et al. 2014, Yau et al. 2018). Indeed FMRP loss is known to affect dendritic spine development in the excitatory neurons in the hippocampus (Sidhu et al. 2014) and mGluR5-dependent LTD in the CA1 hippocampal neurons (Huber et al. 2002). Future studies of changes in electrocortical activity in different areas of the brain using multielectrode array EEGs and the analysis of mouse behaviors following cell- or brain area–specific deletion of FMRP would help us better understand the circuit level mechanisms.

Conclusions

Sensory processing issues are frequently associated with autism, but very little is known about underlying mechanisms. Humans with FXS show consistent and debilitating auditory hypersensitivity. Here, we found that PV+ inhibitory neurons and the ECM structures that cover these cells are affected by *Fmr1* gene deletion in forebrain excitatory neurons, which is likely linked to reduced inhibition, abnormal resting low-gamma EEG power, and hyperactive behaviors. Increased activity of ECM modifying enzyme (MMP-9) may contribute to these deficits by cleaving aggrecan-containing WFA+ PNNs or signaling through cell surface receptors to mTOR/Akt pathway. Gamma synchronization, high-gamma power, and anxiety-like behaviors were unaffected in $Cre^{Nex1}/Fmr1^{Flox/y}$ cKO mice. Together, these findings show that local cortical deficits contribute to many, but not all, phenotypes in the *Fmr1* KO mice and suggest cell type- and circuit-specific contributions of the genetic mutation to various symptoms in FXS. The utility of identifying the relationships between cell type/circuit specificity and phenotypes in neurodevelopmental disorders is that therapeutic approaches can be potentially targeted to impact specific cell types, circuits, and symptoms.

Supplementary Material

Supplementary material is available at *Cerebral Cortex* online.

Funding

National Institute of Child Health and Human Development and the National Institute of Mental Health (1 U54 HD082008-01 to I.M.E., D.K.B., and K.A.R.) and U.S. Army Medical Research and Materiel Command (W81XWH-15-1-0436 and W81XWH-15-1-0434 to I.M.E., D.K.B., and K.A.R.).

Notes

The authors thank Klaus Nave (Göttingen, Germany) and Joshua Sanes (Harvard University) for providing breeding pairs of *Nex1(NeuroD6)*-Cre mice. We thank Dr Christina Gross for her advice on FMRP staining. We also thank Camila Garcia Paz for technical support and members of the Ethell, Binder, and Razak laboratories for helpful discussions and David Carter for advice on confocal microscopy. *Conflict of Interest*: None declared.

References

Anderson LA, Christianson GB, Linden JF. 2009. Mouse auditory cortex differs from visual and somatosensory cortices in the laminar distribution of cytochrome oxidase and acetylcholinesterase. *Brain Res*. 1252:130–142.

Antoine MW, Langberg T, Schnepel P, Feldman DE. 2019. Increased excitation-inhibition ratio stabilizes synapse and circuit excitability in four autism mouse models. *Neuron*. 101:648–661.

Artieda J, Valencia M, Alegre M, Olaziregi O, Urrestarazu E, Iriarte J. 2004. Potentials evoked by chirp-modulated tones: a new technique to evaluate oscillatory activity in the auditory pathway. *Clin Neurophysiol*. 115:699–709.

Atencio CA, Schreiner CE. 2008. Spectrotemporal processing differences between auditory cortical fast-spiking and regular-spiking neurons. *J Neurosci*. 28:3897–3910.

Balakrishnan S, Pearce RA. 2014. Spatiotemporal characteristics and pharmacological modulation of multiple gamma oscillations in the CA1 region of the hippocampus. *Front Neural Circuits*. 8:150.

Ballester-Rosado CJ, Albright MJ, Wu CS, Liao CC, Zhu J, Xu J, Lee LJ, Lu HC. 2010. mGluR5 in cortical excitatory neurons exerts both cell-autonomous and -nonautonomous influences on cortical somatosensory circuit formation. *J Neurosci*. 30:16896–16909.

Balmer TS. 2016. Perineuronal nets enhance the excitability of fast-spiking neurons. *eNeuro*. 3, doi: 10.1523/ENEURO.0112-16.2016.

Beebe K, Wang Y, Kulesza R. 2014. Distribution of fragile X mental retardation protein in the human auditory brainstem. *Neuroscience*. 273:79–91.

Bilousova TV, Dansie L, Ngo M, Aye J, Charles JR, Ethell DW, Ethell IM. 2009. Minocycline promotes dendritic spine maturation and improves behavioural performance in the fragile X mouse model. *J Med Genet*. 46:94–102.

Braat S, Kooy RF. 2015. The GABAA receptor as a therapeutic target for neurodevelopmental disorders. *Neuron*. 86: 1119–1130.

Brown MR, Kronengold J, Gazula VR, Chen Y, Strumbos JG, Sigworth FJ, Navaratnam D, Kaczmarek LK. 2010. Fragile X mental retardation protein controls gating of the sodium-activated potassium channel slack. *Nat Neurosci*. 13:819–821.

Brown RE, Corey SC, Moore AK. 1999. Differences in measures of exploration and fear in MHC-congenic C57BL/6J and B6-H-2K mice. *Behav Genet*. 29:263–271.

Cabungcal JH, Steullet P, Morishita H, Kraftsik R, Cuenod M, Hensch TK, Do KQ. 2013. Perineuronal nets protect fast-spiking interneurons against oxidative stress. *Proc Natl Acad Sci*. 110:9130–9135.

Cardin JA, Carlén M, Meletis K, Knoblich U, Zhang F, Deisseroth K, Tsai LH, Moore CI. 2009. Driving fast-spiking cells induces gamma rhythm and controls sensory responses. *Nature*. 459:663–667.

Carlén M, Meletis K, Siegle JH, Cardin JA, Futai K, Vierling-Claassen D, Rühlmann C, Jones SR, Deisseroth K, Sheng M *et al*. 2012. A critical role for NMDA receptors in parvalbumin interneurons for gamma rhythm induction and behavior. *Mol Psychiatry*. 17:537–548.

Carobrez AP, Bertoglio LJ. 2005. Ethological and temporal analyses of anxiety-like behavior: the elevated plus-maze model 20 years on. *Neuroscience & Biobehavioral Reviews*. 39(8):1193–1205.

Castrén M, Pääkkönen A, Tarkka IM, Ryynänen M, Partanen J. 2003. Augmentation of auditory N1 in children with fragile X syndrome. *Brain Topogr*. 15:165–171.

Chang MC, Park JM, Pelkey KA, Grabenstatter HL, Xu D, Linden DJ, Sutula TP, McBain CJ, Worley PF. 2010. Narp regulates homeostatic scaling of excitatory synapses on parvalbumin-expressing interneurons. *Nat Neurosci*. 13:1090–1097.

Chen L, Toth M. 2001. Fragile X mice develop sensory hyperreactivity to auditory stimuli. *Neuroscience*. 103:1043–1050.

Chen LY, Rex CS, Babayan AH, Kramár EA, Lynch G, Gall CM, Lauterborn JC. 2010. Physiological activation of synaptic Rac>PAK (p-21 activated kinase) signaling is defective in a mouse model of fragile X syndrome. *J Neurosci*. 30:10977–10984.

Christie SB, Akins MR, Schwob JE, Fallon JR. 2009. The FXG: a presynaptic fragile X granule expressed in a subset of developing brain circuits. *J Neurosci*. 29:1514–1524.

Contractor A, Klyachko VA, Portera-Cailliau C. 2015. Altered neuronal and circuit excitability in fragile X syndrome. *Neuron*. 87:699–715.

Crawford DC, Acuña JM, Sherman SL. 2001. FMR1 and the fragile X syndrome: human genome epidemiology review. *Genet Med*. 3:359–371.

d'Ortho MP, Will H, Atkinson S, Butler G, Messent A, Gavrilovic J, Smith B, Timpl R, Zardi L, Murphy G. 1997. Membrane-type matrix metalloproteinases 1 and 2 exhibit broad-spectrum proteolytic capacities comparable to many matrix metalloproteinases. *Eur J Biochem*. 250:751–757.

Dansie LE, Phommahaxay K, Okusanya AG, Uwadia J, Huang M, Rotschafer SE, Razak KA, Ethell DW, Ethell IM. 2013. Long-lasting effects of minocycline on behavior in young but not adult fragile X mice. *Neuroscience*. 246:186–198.

Del Pino I, García-Frigola C, Dehorter N, Brotons-Mas JR, Alvarez-Salvado E, Martínez de Lagrán M, Ciceri G, Gabaldón MV, Moratal D, Dierssen M *et al*. 2013. Erbb4 deletion from fast-spiking interneurons causes schizophrenia-like phenotypes. *Neuron*. 79:1152–1168.

Deng PY, Rotman Z, Blundon JA, Cho Y, Cui J, Cavalli V, Zakharenko SS, Klyachko VA. 2013. FMRP regulates neurotransmitter release and synaptic information transmission by modulating action potential duration via BK channels. *Neuron*. 77:696–711.

Dvorak D, Fenton AA. 2014. Toward a proper estimation of phase-amplitude coupling in neural oscillations. *J Neurosci Methods*. 225:42–56.

Dziembowska M, Pretto DI, Janusz A, Kaczmarek L, Leigh MJ, Gabriel N, Durbin-Johnson B, Hagerman RJ, Tassone F. 2013. High MMP-9 activity levels in fragile X syndrome are lowered by minocycline. *Am J Med Genet A*. 161A:1897–1903.

Dziembowska M, Wlodarczyk J. 2012. MMP9: a novel function in synaptic plasticity. *Int J Biochem Cell Biol*. 44:709–713.

Enriquez-Barreto L, Morales M. 2016. The PI3K signaling pathway as a pharmacological target in autism related disorders and schizophrenia. *Mol Cell Ther*. 4:2.

Ethridge LE, White SP, Mosconi MW, Wang J, Byerly MJ, Sweeney JA. 2016. Reduced habituation of auditory evoked potentials indicate cortical hyper-excitability in fragile X syndrome. *Transl Psychiatry*. 6:e787.

Ethridge LE, White SP, Mosconi MW, Wang J, Pedapati EV, Erickson CA, Byerly MJ, Sweeney JA. 2017. Neural synchronization deficits linked to cortical hyper-excitability and auditory hypersensitivity in fragile X syndrome. *Mol Autism*. 8:22.

Ferron L, Nieto-Rostro M, Cassidy JS, Dolphin AC. 2014. Fragile X mental retardation protein controls synaptic vesicle exocytosis by modulating N-type calcium channel density. *Nat Commun*. 5:3628.

Filice F, Vörckel KJ, Sungur A, Wöhr M, Schwaller B. 2016. Reduction in parvalbumin expression not loss of the parvalbumin-expressing GABA interneuron subpopulation in genetic parvalbumin and shank mouse models of autism. *Mol Brain*. 9:10.

Franklin KB, Paxinos G. 2008. The mouse brain in stereotaxic coordinates. New York (NY): Academic press (vol. 3).

Fu Y, Kaneko M, Tang Y, Alvarez-Buylla A, Stryker MP. 2015. A cortical disinhibitory circuit for enhancing adult plasticity. *Elife*. 4:e05558.

Gabel LA, Won S, Kawai H, McKinney M, Tartakoff AM, Fallon JR. 2004. Visual experience regulates transient expression and dendritic localization of fragile X mental retardation protein. *J Neurosci*. 24:10579–10583.

Garcia-Pino E, Gessele N, Koch U. 2017. Enhanced excitatory connectivity and disturbed sound processing in the auditory brainstem of fragile X mice. *J Neurosci*. 37:7403–7419.

Gibson JR, Bartley AF, Hays SA, Huber KM. 2008. Imbalance of neocortical excitation and inhibition and altered UP states reflect network hyperexcitability in the mouse model of fragile X syndrome. *J Neurophysiol*. 100:2615–2626.

Gkogkas CG, Khoutorsky A, Cao R, Jafarnejad SM, Prager-Khoutorsky M, Giannakas N, Kaminari A, Fragkouli A, Nader K, Price TJ *et al*. 2014. Pharmacogenetic inhibition of eIF4E-dependent Mmp9 mRNA translation reverses fragile X syndrome-like phenotypes. *Cell Rep*. 9:1742–1755.

Goebbels S, Bormuth I, Bode U, Hermanson O, Schwab MH, Nave KA. 2006. Genetic targeting of principal neurons in neocortex and hippocampus of NEX-Cre mice. *Genesis*. 44: 611–621.

Goel A, Cantu DA, Guilfoyle J, Chaudhari GR, Newadkar A, Todisco B, de Alba D, Kourdougli N, Schmitt LM, Pedapati E *et al*. 2018. Impaired perceptual learning in a mouse model of fragile X syndrome is mediated by parvalbumin neuron dysfunction and is reversible. *Nat Neurosci*. 21:1404–1411.

Gonzalez-Burgos G, Lewis DA. 2008. GABA neurons and the mechanisms of network oscillations: implications for understanding cortical dysfunction in schizophrenia. *Schizophr Bull*. 34:944–961.

Gross C, Yao X, Pong DL, Jeromin A, Bassell GJ. 2011. Fragile X mental retardation protein regulates protein expression and mRNA translation of the potassium channel Kv4.2. *J Neurosci*. 31:5693–5698.

Hays SA, Huber KM, Gibson JR. 2011. Altered neocortical rhythmic activity states in Fmr1 KO mice are due to enhanced mGluR5 signaling and involve changes in excitatory circuitry. *J Neurosci*. 31:14223–14234.

Hoeffer CA, Sanchez E, Hagerman RJ, Mu Y, Nguyen DV, Wong H, Whelan AM, Zukin RS, Klann E, Tassone F. 2012. Altered mTOR signaling and enhanced CYFIP2 expression levels in subjects with fragile X syndrome. *Genes Brain Behav*. 11:332–341.

Hou L, Klann E. 2004. Activation of the phosphoinositide 3-kinase-Akt-mammalian target of rapamycin signaling pathway is required for metabotropic glutamate receptor-dependent long-term depression. *J Neurosci*. 24:6352–6361.

Huber KM, Gallagher SM, Warren ST, Bear MF. 2002. Altered synaptic plasticity in a mouse model of fragile X mental retardation. *Proc Natl Acad Sci*. 99:7746–7750.

Hwang JJ, Park MH, Choi SY, Koh JY. 2005. Activation of the Trk signaling pathway by extracellular zinc. Role of metalloproteinases. *J Biol Chem*. 280:11995–12001.

Hébert B, Pietropaolo S, Même S, Laudier B, Laugeray A, Doisne N, Quartier A, Lefeuvre S, Got L, Cahard D *et al*. 2014. Rescue of fragile X syndrome phenotypes in Fmr1 KO mice by a BKCa channel opener molecule. *Orphanet J Rare Dis*. 9:124.

Janusz A, Milek J, Perycz M, Pacini L, Bagni C, Kaczmarek L, Dziembowska M. 2013. The fragile X mental retardation protein regulates matrix metalloproteinase 9 mRNA at synapses. *J Neurosci*. 33:18234–18241.

Kazdoba TM, Sunnen CN, Crowell B, Lee GH, Anderson AE, D'Arcangelo G. 2012. Development and characterization of NEX-Pten, a novel forebrain excitatory neuron-specific knockout mouse. *Dev Neurosci*. 34:198–209.

Keeley S, Fenton AA, Rinzel J. 2017. Modeling fast and slow gamma oscillations with interneurons of different subtype. *J Neurophysiol*. 117:950–965.

Kerrisk ME, Greer CA, Koleske AJ. 2013. Integrin α3 is required for late postnatal stability of dendrite arbors, dendritic spines and synapses, and mouse behavior. *J Neurosci*. 33: 6742–6752.

Kim H, Gibboni R, Kirkhart C, Bao S. 2013. Impaired critical period plasticity in primary auditory cortex of fragile X model mice. *J Neurosci*. 33:15686–15692.

Klann E, Dever TE. 2004. Biochemical mechanisms for translational regulation in synaptic plasticity. *Nat Rev Neurosci*. 5:931–942.

Legate KR, Wickström SA, Fässler R. 2009. Genetic and cell biological analysis of integrin outside-in signaling. *Genes Dev*. 23:397–418.

Lensjø KK, Lepperød ME, Dick G, Hafting T, Fyhn M. 2017. Removal of Perineuronal nets unlocks juvenile plasticity through network mechanisms of decreased inhibition and increased gamma activity. *J Neurosci*. 37:1269–1283.

Lovelace JW, Ethell IM, Binder DK, Razak KA. 2018. Translation-relevant EEG phenotypes in a mouse model of fragile X syndrome. *Neurobiol Dis*. 115:39–48.

Lovelace JW, Wen TH, Reinhard S, Hsu MS, Sidhu H, Ethell IM, Binder DK, Razak KA. 2016. Matrix metalloproteinase-9 deletion rescues auditory evoked potential habituation deficit in a mouse model of fragile X syndrome. *Neurobiol Dis*. 89:126–135.

Lucas EK, Markwardt SJ, Gupta S, Meador-Woodruff JH, Lin JD, Overstreet-Wadiche L, Cowell RM. 2010. Parvalbumin deficiency and GABAergic dysfunction in mice lacking PGC-1α. *J Neurosci*. 30:7227–7235.

Maris E, Oostenveld R. 2007. Nonparametric statistical testing of EEG- and MEG-data. *J Neurosci Methods*. 164:177–190.

Martin del Campo HN, Measor KR, Razak KA. 2012. Parvalbumin immunoreactivity in the auditory cortex of a mouse model of presbycusis. *Hear Res*. 294:31–39.

McRae PA, Baranov E, Sarode S, Brooks-Kayal AR, Porter BE. 2010. Aggrecan expression, a component of the inhibitory interneuron perineuronal net, is altered following an early-life seizure. *Neurobiol Dis*. 39:439–448.

McRae PA, Rocco MM, Kelly G, Brumberg JC, Matthews RT. 2007. Sensory deprivation alters aggrecan and perineuronal net expression in the mouse barrel cortex. *J Neurosci*. 27:5405–5413.

Mientjes EJ, Nieuwenhuizen I, Kirkpatrick L, Zu T, Hoogeveen-Westerveld M, Severijnen L, Rifé M, Willemsen R, Nelson DL, Oostra BA. 2006. The generation of a conditional Fmr1 knock out mouse model to study Fmrp function in vivo. *Neurobiol Dis*. 21:549–555.

Miyata S, Kitagawa H. 2016. Chondroitin 6-sulfation regulates perineuronal net formation by controlling the stability of aggrecan. *Neural Plast*. 2016:1305801.

Moore AK, Wehr M. 2013. Parvalbumin-expressing inhibitory interneurons in auditory cortex are well-tuned for frequency. *Journal of Neuroscience* 33:13713–13723.

Morawski M, Brückner G, Arendt T, Matthews RT. 2012. Aggrecan: beyond cartilage and into the brain. *Int J Biochem Cell Biol*. 44:690–693.

Murase S, Lantz CL, Kim E, Gupta N, Higgins R, Stopfer M, Hoffman DA, Quinlan EM. 2016. Matrix metalloproteinase-9 regulates neuronal circuit development and excitability. *Mol Neurobiol*. 53:3477–3493.

Myrick LK, Deng PY, Hashimoto H, Oh YM, Cho Y, Poidevin MJ, Suhl JA, Visootsak J, Cavalli V, Jin P *et al*. 2015. Independent role for presynaptic FMRP revealed by an FMR1 missense

mutation associated with intellectual disability and seizures. *Proc Natl Acad Sci*. 112:949–956.

Niell CM, Stryker MP. 2010. Modulation of visual responses by behavioral state in mouse visual cortex. *Neuron*. 65:472–479.

Nielsen DM, Derber WJ, McClellan DA, Crnic LS. 2002. Alterations in the auditory startle response in Fmr1 targeted mutant mouse models of fragile X syndrome. *Brain Res*. 927: 8–17.

Ozeki H, Finn IM, Schaffer ES, Miller KD, Ferster D. 2009. Inhibitory stabilization of the cortical network underlies visual surround suppression. *Neuron*. 62:578–592.

Packer AM, Yuste R. 2011. Dense, unspecific connectivity of neocortical parvalbumin-positive interneurons: a canonical microcircuit for inhibition? *J Neurosci*. 31:13260–13271.

Patz S, Grabert J, Gorba T, Wirth MJ, Wahle P. 2004. Parvalbumin expression in visual cortical interneurons depends on neuronal activity and TrkB ligands during an early period of postnatal development. *Cereb Cortex*. 14:342–351.

Penagarikano O, Mulle JG, Warren ST. 2007. The pathophysiology of fragile x syndrome. *Annu Rev Genomics Hum Genet*. 8:109–129.

Pizzorusso T, Medini P, Berardi N, Chierzi S, Fawcett JW, Maffei L. 2002. Reactivation of ocular dominance plasticity in the adult visual cortex. *Science*. 298:1248–1251.

Purcell DW, John SM, Schneider BA, Picton TW. 2004. Human temporal auditory acuity as assessed by envelope following responses. *J Acoust Soc Am*. 116:3581–3593.

Pérez-Alcázar M, Nicolás MJ, Valencia M, Alegre M, Iriarte J, Artieda J. 2008. Chirp-evoked potentials in the awake and anesthetized rat. A procedure to assess changes in cortical oscillatory activity. *Exp Neurol*. 210:144–153.

Radwan B, Dvorak D, Fenton AA. 2016. Impaired cognitive discrimination and discoordination of coupled theta–gamma oscillations in Fmr1 knockout mice. *Neurobiol Dis*. 88:125–138.

Rais M, Binder DK, Razak KA, Ethell IM. 2018. Sensory processing phenotypes in fragile X syndrome. *ASN Neuro*. 10:1759091418801092.

Ray S, Maunsell JH. 2011. Different origins of gamma rhythm and high-gamma activity in macaque visual cortex. *PLoS Biol*. 9:e1000610.

Rojas DC, Benkers TL, Rogers SJ, Teale PD, Reite ML, Hagerman RJ. 2001. Auditory evoked magnetic fields in adults with fragile X syndrome. *Neuroreport*. 12:2573–2576.

Ronesi JA, Huber KM. 2008. Homer interactions are necessary for metabotropic glutamate receptor-induced long-term depression and translational activation. *J Neurosci*. 28:543–547.

Rotschafer S, Razak K. 2013. Altered auditory processing in a mouse model of fragile X syndrome. *Brain Res*. 1506:12–24.

Rotschafer SE, Marshak S, Cramer KS. 2015. Deletion of Fmr1 alters function and synaptic inputs in the auditory brainstem. *PLoS One*. 10:e0117266.

Rotschafer SE, Razak KA. 2014. Auditory processing in fragile x syndrome. *Front Cell Neurosci*. 8:19.

Rotschafer SE, Trujillo MS, Dansie LE, Ethell IM, Razak KA. 2012. Minocycline treatment reverses ultrasonic vocalization production deficit in a mouse model of fragile X syndrome. *Brain Res*. 1439:7–14.

Roughley PJ, Mort JS. 2014. The role of aggrecan in normal and osteoarthritic cartilage. *J Exp Orthop*. 1:8.

Santos AR, Kanellopoulos AK, Bagni C. 2014. Learning and behavioral deficits associated with the absence of the fragile X mental retardation protein: what a fly and mouse model can teach us. *Learn Mem*. 21:543–555.

Sato A. 2016. mTOR, a potential target to treat autism spectrum disorder. *CNS Neurol Disord Drug Targets*. 15:533–543.

Schneider A, Leigh MJ, Adams P, Nanakul R, Chechi T, Olichney J, Hagerman R, Hessl D. 2013. Electrocortical changes associated with minocycline treatment in fragile X syndrome. *J Psychopharmacol*. 27:956–963.

Selby L, Zhang C, Sun QQ. 2007. Major defects in neocortical GABAergic inhibitory circuits in mice lacking the fragile X mental retardation protein. *Neurosci Lett*. 412:227–232.

Sharma A, Hoeffer CA, Takayasu Y, Miyawaki T, McBride SM, Klann E, Zukin RS. 2010. Dysregulation of mTOR signaling in fragile X syndrome. *J Neurosci*. 30:694–702.

Sidhu H, Dansie LE, Hickmott PW, Ethell DW, Ethell IM. 2014. Genetic removal of matrix metalloproteinase 9 rescues the symptoms of fragile X syndrome in a mouse model. *J Neurosci*. 34:9867–9879.

Sinclair D, Oranje B, Razak KA, Siegel SJ, Schmid S. 2017. Sensory processing in autism spectrum disorders and fragile X syndrome-from the clinic to animal models. *Neurosci Biobehav Rev*. 76:235–253.

Sohal VS, Zhang F, Yizhar O, Deisseroth K. 2009. Parvalbumin neurons and gamma rhythms enhance cortical circuit performance. *Nature*. 459:698–702.

Strumbos JG, Brown MR, Kronengold J, Polley DB, Kaczmarek LK. 2010. Fragile X mental retardation protein is required for rapid experience-dependent regulation of the potassium channel Kv3.1b. *J Neurosci*. 30:10263–10271.

Sutcliffe JS, Nelson DL, Zhang F, Pieretti M, Caskey CT, Saxe D, Warren ST. 1992. DNA methylation represses FMR-1 transcription in fragile X syndrome. *Hum Mol Genet*. 1:397–400.

Szklarczyk A, Lapinska J, Rylski M, McKay RD, Kaczmarek L. 2002. Matrix metalloproteinase-9 undergoes expression and activation during dendritic remodeling in adult hippocampus. *J Neurosci*. 22:920–930.

Tallon-Baudry C, Bertrand O, Delpuech C, Pernier J. 1996. Stimulus specificity of phase-locked and non-phase-locked 40 Hz visual responses in human. *J Neurosci*. 16:4240–4249.

Tamamaki N, Yanagawa Y, Tomioka R, Miyazaki J, Obata K, Kaneko T. 2003. Green fluorescent protein expression and colocalization with calretinin, parvalbumin, and somatostatin in the GAD67-GFP knock-in mouse. *J Comp Neurol*. 467:60–79.

Tranfaglia MR. 2011. The psychiatric presentation of fragile x: evolution of the diagnosis and treatment of the psychiatric comorbidities of fragile X syndrome. *Dev Neurosci*. 33:337–348.

Tsodyks MV, Skaggs WE, Sejnowski TJ, McNaughton BL. 1997. Paradoxical effects of external modulation of inhibitory interneurons. *J Neurosci*. 17:4382–4388.

Veit J, Hakim R, Jadi MP, Sejnowski TJ, Adesnik H. 2017. Cortical gamma band synchronization through somatostatin interneurons. *Nat Neurosci*. 20:951–959.

Verkerk AJ, Pieretti M, Sutcliffe JS, Fu YH, Kuhl DP, Pizzuti A, Reiner O, Richards S, Victoria MF, Zhang FP. 1991. Identification of a gene (FMR-1) containing a CGG repeat coincident with a breakpoint cluster region exhibiting length variation in fragile X syndrome. *Cell*. 65:905–914.

Volman V, Behrens MM, Sejnowski TJ. 2011. Downregulation of parvalbumin at cortical GABA synapses reduces network gamma oscillatory activity. *J Neurosci*. 31:18137–18148.

Wang J, Ethridge LE, Mosconi MW, White SP, Binder DK, Pedapati EV, Erickson CA, Byerly MJ, Sweeney JA. 2017. A resting EEG study of neocortical hyperexcitability and altered functional connectivity in fragile X syndrome. *J Neurodev Disord*. 9:11.

Wang Y, Sakano H, Beebe K, Brown MR, de Laat R, Bothwell M, Kulesza RJ, Rubel EW. 2014. Intense and specialized dendritic localization of the fragile X mental retardation protein in binaural brainstem neurons: a comparative study in the alligator, chicken, gerbil, and human. *J Comp Neurol*. 522:2107–2128.

Wen TH, Afroz S, Reinhard SM, Palacios AR, Tapia K, Binder DK, Razak KA, Ethell IM. 2018a. Genetic reduction of matrix Metalloproteinase-9 promotes formation of perineuronal nets around Parvalbumin-expressing interneurons and normalizes auditory cortex responses in developing Fmr1 Knock-out mice. *Cereb Cortex*. 28:3951–3964.

Wen TH, Binder DK, Ethell IM, Razak KA. 2018b. The Perineuronal 'Safety' net? Perineuronal net abnormalities in neurological disorders. *Front Mol Neurosci*. 11:270.

Yan QJ, Asafo-Adjei PK, Arnold HM, Brown RE, Bauchwitz RP. 2004. A phenotypic and molecular characterization of the fmr1-tm1Cgr fragile X mouse. *Genes Brain Behav*. 3: 337–359.

Yan QJ, Rammal M, Tranfaglia M, Bauchwitz RP. 2005. Suppression of two major fragile X syndrome mouse model phenotypes by the mGluR5 antagonist MPEP. *Neuropharmacology*. 49:1053–1066.

Yau SY, Bettio L, Vetrici M, Truesdell A, Chiu C, Chiu J, Truesdell E, Christie BR. 2018. Chronic minocycline treatment improves hippocampal neuronal structure, NMDA receptor function, and memory processing in Fmr1 knockout mice. *Neurobiol Dis*. 113:11–22.

Yang F, Je HS, Ji Y, Nagappan G, Hempstead B, Lu B. 2009. Pro-BDNF-induced synaptic depression and retraction at developing neuromuscular synapses. *J Cell Biol*. 185:727–741.

Yong VW, Krekoski CA, Forsyth PA, Bell R, Edwards DR. 1998. Matrix metalloproteinases and diseases of the CNS. *Trends Neurosci*. 21:75–80.

Zhang Y, Brown MR, Hyland C, Chen Y, Kronengold J, Fleming MR, Kohn AB, Moroz LL, Kaczmarek LK. 2012. Regulation of neuronal excitability by interaction of fragile X mental retardation protein with slack potassium channels. *J Neurosci*. 32:15318–15327.

Zorio DA, Jackson CM, Liu Y, Rubel EW, Wang Y. 2017. Cellular distribution of the fragile X mental retardation protein in the mouse brain. *J Comp Neurol*. 525:818–849.